TITLE

Climate-driven unsteady denudation and sediment flux in a high-relief unglaciated catchment-fan using ^{26}Al and ^{10}Be: Panamint Valley, California

AUTHORS

Cody C. Mason* and Brian W. Romans

Department of Geosciences, Virginia Tech, Blacksburg, Virginia, 24061

*Corresponding Author: Cody C. Mason

Email: cmason80@vt.edu

KEYWORDS

Sediment Routing System, Catchment-fan, Signal Propagation, Paleodenudation, Climate, Cosmogenic Radionuclides

HIGHLIGHTS

- $^{26}Al/^{10}Be$ Burial ages/paleodenudation rates measured in early to middle Pleistocene alluvium
- Denudation variability of +50/-33% from mean rate in unglaciated catchment-fan
- High-frequency changes suggest multi-millennial timescale climatic forcing
- 100 kyr Milankovitch periods may drive observable variability in CRN concentrations
- Limitations of $^{26}Al/^{10}Be$ method applied to alluvial fan stratigraphy are discussed

ABSTRACT

Empirical models and numerical simulations of coupled erosional-depositional sedimentary systems make specific predictions for relationships between changing catchment boundary conditions and sediment fluxes to depositional segments. However, testing whether changes in catchment boundary conditions modulate sediment flux in natural systems over multi-millennial timescales proves challenging because of a lack of methods to quantify sediment flux from stratigraphy. Tectonic and climatic boundary conditions in the Panamint Range, California, are relatively well-constrained by existing thermochronology and regional multi-proxy paleoclimate studies, respectively, and catchment-fan systems present there minimize sediment storage and recycling, offering an excellent natural laboratory to test conceptual models of climate-sedimentary dynamics. We used stratigraphic characterization and cosmogenic radionuclides (CRNs; ^{26}Al & ^{10}Be) in the Pleasant Canyon complex (PCC), a linked catchment-fan system, to examine the effects of Pleistocene high-magnitude, high-frequency climate change on CRN-derived denudation rates and sediment flux in a high-relief, unglaciated catchment-fan system. Calculated ^{26}Al/^{10}Be burial ages from 13 samples collected in an ~180 m thick outcropping stratigraphic succession range from ca. 1.55 ± 0.16 Ma in basal strata, to ca. 0.33 ± 0.14 Ma – 0.65 ± 0.22 Ma at ~18 m below the abandoned fan surface. The mean long-term CRN-derived paleodenudation rate, 36 ± 8 mm/kyr (1σ), is higher than the modern rate of 24 ± 0.6 mm/kyr from Pleasant Canyon, and paleodenudation rates between ca. 0.33 – 0.70 Ma display high-frequency variability in the high end (up to 54 mm/kyr). The highest CRN-derived denudation rates/sediment fluxes are associated with stratigraphic evidence for increased precipitation during glacial-pluvial times, and occur after the transition to 100 kyr climatic periodicity (post mid-Pleistocene transition, or ca. 750 ka). We employed end-member mixing models to examine the potential for unsteady catchment processes to contribute to apparent denudation variability;

results suggest that a mixture of >50% low-CRN-concentration sediment is required to produce CRN-concentrations that result in the observed increases in apparent denudation. The overall pattern of CRN-derived burial ages, paleodenudation rates, and stratigraphic facies suggests that climate transitions drove the observed variability in catchment denudation and sediment flux in this unglaciated catchment-fan system.

1.0 INTRODUCTION

Sediment routing systems consist of an erosional zone, a fluvial transfer zone, and a depositional basin (Allen, 2008). The creation and preservation of stratigraphy within a sediment routing system is the sum of complex processes including up-system environmental changes in the erosion zone, sediment storage and recycling in the erosion or fluvial transfer zones, and changes in accommodation and intrinsic system dynamics in depositional basins (Paola et al., 1992). Some geoscientists have conceptualized sediment production, transport, storage, and remobilization dynamics along sediment routing systems in terms of environmental signal propagation (Castelltort and Van Den Driessche, 2003; Romans et al., 2016). In this framework, signal to noise ratio, signal delay, signal attenuation, or signal 'shredding' may preclude preservation or inversion of up-system environmental change from depositional products found in sedimentary basins (Jerolmack and Paola, 2010; Romans et al., 2016). Given this context, *a priori* assumptions of minimal signal delay, attenuation, or shredding are required to invert or explore effects of up-system drivers on magnitude and variability of signals of erosion-deposition dynamics. A steep catchment-fan system with a continuously subsiding depositional segment represents an ideal natural laboratory for the investigation of sedimentary signal propagation because: (1) it may react rapidly to changes in boundary conditions, (2) it likely experiences minimal signal delay or attenuation because it lacks, or has a very short transfer zone, and (3) rapidly subsiding alluvial basins contain relatively complete records of past surface dynamics (Straub and Esposito, 2013). Catchment-fan systems have previously been used to explore effects of environmental change on catchment erosion, sediment flux, and sediment caliber exiting catchments (Fig. 1) (Allen and Densmore, 2000; Densmore et al., 2007; Armitage et al., 2011). In such a framework, changes in catchment-scale erosion and sediment flux from catchment to fan are direct signals of up-system environmental change. A fundamental question then is what are the magnitudes of signals emitted from the erosive source of a natural catchment-fan system? And a related question is by how much do such magnitudes vary through time? Placing constraints on denudation rate variability—a proxy for sediment supply at a catchment outlet—through time, in a single sediment routing system, allows for the examination of signals of environmental change.

Predicting catchment response to environmental change, specifically climatic transitions, on a global to individual catchment basis is challenging, because with several exceptions there is a lack of empirical data sets that constrain high-resolution and long-term ($10^{3\text{-}4}$ yr and 10^6 yr, respectively) records of changes in catchment-scale erosion or sediment flux (Granger and Schaller, 2014; Puchol et al., 2016; Oskin et al., 2017). Researchers have addressed this topic by measuring CRNs in alluvial and lacustrine stratigraphy to derive a time series of paleodenudation rates (Balco and Stone, 2005; Granger and Schaller, 2014), by utilizing volumetric estimates of basin fill (Covault et al., 2011), or by analyzing provenance of dated sedimentary deposits spanning climatic changes (Mason et al., 2017). Results indicate many glaciated sediment routing systems have responded to changing climatic boundary conditions, often within resolution of the various chronometers (Stock et al., 2005; Glotzbach et al., 2013; Marshall et al., 2015; Gulick et al., 2015; Mason et al., 2017), whereas many records from glaciated and unglaciated systems show a complex response, or a lack of any measurable change in denudation rate or fluxes to basins across major climate transitions (Granger et al., 2001; Oskin et al., 2017). For instance, in the Tibetan Plateau, ^{10}Be-derived denudation rates across the Plio-Pleistocene transition show a complex, asynchronous, or weak transient response to onset of glaciation (Puchol et al., 2016). In the unglaciated Peninsular Ranges of southern California, ^{10}Be-derived paleodenudation rates across the Plio-Pleistocene transition (ca. 4 – 1 Ma) remained constant (Oskin et al., 2017). However, in the unglaciated Northern Kenya Rift erosion/deposition rates saw a significant transient increase during the African Humid Period, between ca. 5 – 15 ka, (Garcin et al., 2017), and tectonically quiescent, unglaciated sediment routing systems along the Texas Gulf Coast responded to interglacial warm periods with increased CRN-derived denudation rates (Hidy et. al., 2014). Yet in the Pacific Northwest, periglacial conditions during the last glacial maximum increased CRN-derived denudation rates relative to the Holocene (Marshall et al., 2015). These results highlight the complexity in natural system response to changing climate, complicate interpretations of sedimentary records of environmental change, and prediction of system response to future global climate change.

Numerical simulations of linked catchment-fan systems represent a tool to bridge the gap between modern and geologic-timescale empirical studies, and may be used to explore effects of up-system forcings on depositional products. Simulations typically impose changes in catchment or orogen-scale boundary conditions—often precipitation and fault-slip rate (Fig. 1)—and measure various model outputs including channel incision rate, catchment denudation, sediment flux at catchment outlets, and spatial distribution of grain-size variations in the depositional segment (Allen and Densmore, 2000; Armitage et al., 2011). Such studies predict distinct timescales of system response and equilibrium for various forcings, with reaction timescales to perturbations in precipitation occurring over ~10^{3-4} yrs, and reaction timescales to tectonic perturbations occurring over 10^{5-6} yrs (Fig. 1) (Allen, 2008; Armitage et al., 2011). Crucially, models that modulate precipitation rates mimicking Milankovitch-timescale climate change result in concomitant modulation of catchment denudation rates and sediment fluxes (Allen and Densmore, 2000). To test the predictions of numerical models in natural systems, two fundamental conditions must be met: (1) paleoclimatic and tectonic boundary conditions should be relatively well constrained, and (2) the system must preserve a stratigraphic record of changes in denudation rates, sediment flux, or depositional volumes through time.

In this paper, we place new constraints on CRN-derived signals of denudation rate variability over multi-millennial timescales in a steep, unglaciated, catchment-fan system within an uplifted normal fault block in Panamint Valley, California. This configuration is common to much of the American Great Basin, Basin and Range of the United States and Mexico, and elsewhere globally, yet is underrepresented in existing literature. We present new data and interpretations from 13 CRN samples collected throughout a 180-m thick succession of outcropping Pleistocene alluvial-lacustrine strata, and from two samples of modern sediment collected at feeder catchment outlets. This empirical record of CRN-derived denudation rate and sediment supply, as stored in the depositional segment of a linked catchment-fan, represents a test of conceptual, numerical, and empirically derived predictions for the effects of multi-millennial timescale climate change on catchment-erosion and fan-deposition dynamics.

2.0 BACKGROUND

2.1 Pleasant Canyon Complex Source-to-Sink Parameters

The Panamint Range and Valley are located in eastern California, west of Death Valley and east of the Argus and Slate Ranges (Fig. 2). The Pleasant Canyon complex (PCC) lies at the terminus of a high-relief catchment (~2350 meters) that drains 32.8 km^2 of the central Panamint Range. Figure 3 displays catchment parameters including elevation, surface slope, geology and hypsometry for Pleasant Canyon. The bedrock lithologies of Pleasant Canyon are primarily quartz-bearing Proterozoic-aged metamorphic, igneous, and sedimentary units, with the exception of restricted exposures of the Sentinel Peak member of the Noonday Dolomite (Fig. 3c) (Albee et al., 1981). The contact between World Beater Gneiss and Proterozoic sedimentary units in the upper reaches of Pleasant Canyon (Figure 3c) corresponds to a decrease in slope associated with minor Pleistocene to Holocene alluvial deposits (Albee et al., 1981).

The exhumed depositional segment of the PCC is positioned at the mouth of Pleasant Canyon (Figs. 2 and 3) and is composed of ~180 m of mixed alluvial and lacustrine deposits of Pleistocene age (Smith, 1976; Vogel et al., 2002). Stratigraphic surfaces in the PCC were once active alluvial fan, subaqueous lake bed, or playa floor environments. Deposits aggraded during progressive burial via tectonic subsidence, followed by Pleistocene exhumation and inversion along a series of high-angle normal faults known as the Panamint Valley fault zone (Fig. 2) (Cichanski, 2000; Vogel et al. 2002). Unfortunately, the timing of localized high-angle faulting and inversion of PCC deposits is constrained only by the unknown age of the youngest abandoned alluvial fan surfaces. Small headward eroding gullies have formed since exhumation, and now afford excellent 3-D exposures of PCC stratigraphy.

2.2 Late Cenozoic Tectonic History

The tectonic history of the Panamint Mountains is a first-order control on the pace of catchment denudation and sediment flux to linked alluvial fans (Allen and Densmore, 2000). The Panamint Mountains (Fig. 2) are located within the eastern California-Walker Lane shear zone, a region of diffuse dextral plate boundary deformation east of the San Andreas fault. Panamint Valley is defined by active structures displaying complex Plio-Quaternary deformation patterns; eastern Panamint Valley is bound by the low-angle Panamint-Emigrant detachment system exposed along, or at low elevation within, the Panamint range front (Fig. 2). Active deformation is potentially mainly accommodated by a second set of high-angle oblique dextral faults, the Panamint Valley fault zone, which has cut and displaced Pleistocene to Holocene alluvium exposed along eastern Panamint Valley and the western Panamint range-front (Fig. 2; Cichanski, 2000). The western Panamint Valley is structurally bound by the dextral-oblique Ash Hill fault system near the eastern foot of the Argus Range (Fig. 2) (Densmore and Anderson, 1997).

Early tectonic exhumation and uplift of the Panamint Mountains may have initiated along a single west-dipping, west-side-down, master detachment fault—the Panamint-Emigrant detachment fault (Fig. 2)—starting close to ca. 12 Ma (Bidgoli et al., 2015). Low-temperature thermochronometry (zircon U-Th/He) from the central Panamint Range shows exhumation-related cooling initiated after ca. 12 Ma, while lower temperature thermochronometers (apatite U-Th/He) cluster at ca. 4 Ma, and support rapid Pliocene cooling and tectonic exhumation of the Panamint Range, potentially associated with the initiation of the dextral oblique Panamint Valley fault zone (Bidgoli et al., 2015). Sediment accumulation within the Nova Basin in northeast Panamint Valley occurred between ca. 4.4 – 3 Ma, consistent with Pliocene tectonic rejuvenation (Fig. 2) (Snyder and Hodges, 2000).

Pleistocene to recent rates of dip-slip motion for the Panamint Valley fault zone near Ballarat are ~0.35 – 1 mm/yr (Fig. 2), and were derived using detrital zircon maximum depositional ages from basal stratigraphy of the PCC (Vogel et al., 2002). Dextral deformation rates along the Panamint Valley fault zone are debated, but are thought to be between 1 – 4 mm/yr (Smith, 1976; Oswald and Wesnousky, 2002). Given available information, early to middle Pleistocene catchment denudation rates should reflect equilibrium with respect to uplift patterns of the central Panamint Range since ca. 3 – 4 Ma (Fig. 1) (Allen and Densmore, 2000; Densmore et al., 2007; Armitage et al., 2011).

2.3 Pleistocene Climate History

Panamint Valley is an arid to semi-arid endorheic basin located in a major rain shadow east of the Sierra Nevada Range. Precipitation is scarce at low elevations in Panamint Valley, but increases with elevation in a semi-logarithmic manner in the Panamint Range (Jayko, 2005). The Wildrose Ranger station (1250 m asl) in the northern Panamint Range receives an average of 19 cm of precipitation annually (Jayko, 2005). No long-term record of precipitation exists for Pleasant Canyon, but the mean elevation of ~1700 m asl likely results in >25 – 35 cm of mean annual precipitation. Observations of modern sedimentation events in Death and Panamint Valley indicate catchment hillslopes and fluvial channels transmit material to alluvial fans during low-frequency, high-magnitude storm events. Thus, long-term trends in major storm frequency may influence sediment transfer from catchment to fan.

Pleistocene climate in the Great Basin was on average wetter and colder than the late Holocene interglacial (See inset map from Fig. 2; Oster et al., 2015). Pluvial lakes filled Panamint Valley multiple times during the Pleistocene (Smith, 1976) via increased local precipitation and runoff from the paleo Owens River system (Jannik et al., 1991; Phillips, 2008). Continental paleoclimate records including pollen, hydrological restorations of pluvial lakes, oxygen isotope data, and mass-balance models of Pleistocene Sierra Nevada glaciers agree that temperatures during the last glacial maximum were ~5 – 6°C colder, and precipitation was up to 2x greater than during the late Holocene (D'Arcy et al., 2016, and references therein). Mid-glacial climate conditions typify most of the Pleistocene, and were 2 – 3°C colder with precipitation rates ~1.5x those of modern conditions (D'Arcy et al., 2016). D'Arcy et al. (2016) found that Late Pleistocene climatic forcing, specifically increased precipitation, resulted in measurable differences in patterns of down-system fining of alluvial sediments on Death Valley fans. However, estimates for changes in erosion rate and total fluxes from catchment to fan over glacial-interglacial timescales remain unresolved.

2.4 Previous Regional Paleodenudation Studies

The ages of alluvial fans in the Death Valley area have been used to understand rates of tectonic deformation and effects of climate on alluvial fan morphology (Frankel et al., 2007). Unfortunately, few employed catchment-wide paleodenudation rate techniques. Frankel et al. (2007) dated faulted alluvial fans in northern Death Valley using ^{36}Cl depth profiles, and used inherited concentrations to derive paleodenudation rates of ~40 and ~80 mm/kyr for two catchment-fan systems along the western Grapevine Mountains during the last mid-glacial (ca. 70 ± 10 ka).

Alluvial fan volumetric estimates and rough age constraints were used to quantify time-averaged denudation rates for catchments along the western Panamint Range; results suggest rates between ~40 – 230 mm/kyr. Jayko (2005) used these results to suggest higher precipitation may lead to higher sediment flux in the western Panamint Range. We note that differential slip rates along the range-bounding faults would play a fundamental role in controlling relief and slope, both of which may correlate positively to higher denudation rates. A time series of denudation rates from a single high-relief, unglaciated catchment within the Great Basin represents a crucial missing component to understanding variability of erosion-deposition dynamics across glacial-interglacial climate transitions.

3.0 METHODS

3.1 Sedimentary Lithofacies & Stratigraphic Architecture

We characterized the stratigraphy of the PCC using measured lithostratigraphic sections, and high-resolution photopanoramas for inaccessible outcrops. For our two measured sections (Fig. 2b), stratigraphy and sedimentology were characterized at the cm to decimeter scale. We recorded dominant grain size, bed thickness, sedimentary structures, sorting, particle roundness, clast vs. matrix support, and lateral continuity of beds, and constructed lithofacies and lithofacies associations that were used to interpret depositional environments (See Supplementary material S2).

3.2 Field Sampling, Laboratory Preparation, and Measurement of Cosmogenic $^{26}Al/^{10}Be$

We took advantage of the linked nature of the Pleasant Canyon catchment-fan system by collecting quartz-rich sediment in a vertical succession from Pleistocene alluvium derived directly from Pleasant Canyon. Samples taken vertically through a stratigraphic succession represent a record of catchment denudation rates through time (*e.g.* Balco and Stone, 2005). All samples were located within, or stratigraphically correlated to our measured sections (locations depicted in Fig. 2b).

Our sampling strategy was designed to minimize effects of modern exposure to cosmic rays (similar to that of Puchol et al., 2017; Oskin et al., 2017). We collected sediment from well-shielded vertical or overhanging canyon walls, mostly within narrow canyons. In each case, sediment was excavated from a horizontal depth of at least 50 cm into outcrops, parallel to bedding. We sieved sediment in the field and collected the medium sand-sized fraction (250 – 500 μm). A total of 15 samples were collected during this study; 13 samples were collected from outcrop, and 2 samples were collected from modern wash sediment at catchment outlets. Our goal was to quantify both catchment-averaged paleodenudation in Pleasant Canyon through time, and to quantify the modern catchment-averaged denudation rate.

Samples of Pleistocene and modern sediment underwent standard physical separation and chemical purification procedures at the Purdue Rare Isotope Measurement Laboratory (PRIME Lab). Samples were washed and wet sieved to remove fine particles, then underwent a technique of froth-floatation to separate quartz from feldspar. Samples underwent magnetic separation and were then treated with heavy liquids to isolate quartz. Purified quartz was then leached in dilute HF-HNO_3 baths in an ultrasonic tank to remove the meteoric CRN components. All samples of pure quartz were screened using inductively coupled plasma optical emission spectrometry (ICP-OES). Samples of pure quartz were spiked with ^{27}Al or ^{9}Be carrier of known concentration, and dissolved using concentrated HF/HNO_3. Samples were then filtered through cation and anion exchange columns, then Al and Be hydroxides were dried and converted to oxides, and loaded into targets to be measured using accelerator mass spectrometry (AMS) at the PRIME Lab. AMS results were corrected using blank concentrations following standard PRIME Lab procedures (See Supplementary Table 1 for complete sample and blank measurements).

3.3 Cosmogenic $^{26}Al/^{10}Be$ Burial Dating and Paleodenudation Calculations

Quartz sediment eroded from a catchment and mixed in a fluvial system retains a concentration of CRNs (^{26}Al and ^{10}Be) inversely proportional to the spatially averaged denudation rate within that catchment (Lal, 1991; Bierman and Steig, 1996; Granger and Muzikar, 2001). Consequently, rapidly eroding landscapes result in low concentrations of CRNs in fluvial sediment, while the opposite is true for slowly eroding landscapes. Sediment in catchment-fan systems is evacuated and rapidly deposited on the fan surface, and assuming the pre-burial concentration of CRN found in sediment is due to steady vertical advection during erosion, the concentration ($N_{Al,Be}$ in atoms/g SiO_2) is simply a function of the erosion rate (E) in cm/yr:

$$(1)\ N_{Al}\ (0) = \frac{A_0}{\frac{1}{\tau_{Al}} + \frac{E}{L_0}} + \frac{A_1}{\frac{1}{\tau_{Al}} + \frac{E}{L_1}} + \frac{A_2}{\frac{1}{\tau_{Al}} + \frac{E}{L_2}} + \frac{A_3}{\frac{1}{\tau_{Al}} + \frac{E}{L_3}}$$

$$(2)\ N_{Be}\ (0) = \frac{B_0}{\frac{1}{\tau_{Be}} + \frac{E}{L_0}} + \frac{B_1}{\frac{1}{\tau_{Be}} + \frac{E}{L_1}} + \frac{B_2}{\frac{1}{\tau_{Be}} + \frac{E}{L_2}} + \frac{B_3}{\frac{1}{\tau_{Be}} + \frac{E}{L_3}}$$

Where A_j and B_j are coefficients, with values of A_0 = 28.5, A_1 = 0.72. A_2 = 0.16, A_3 = 0.19, B_0 = 4, B_1 = 0.09, B_2 = 0.02, and B_3 = 0.02, and in units of atoms/yr/g SiO_2, (Granger and Muzikar, 2001; Borchers et al., 2016). L_j represents an attenuation length scale for CRN production reactions; L_0 refers to the attenuation length for spallogenic reactions, L_1 and L_2 are attenuation lengths for negative muon capture, and L_3 is the attenuation length for fast muon capture. We assign values of $L_0 = 160/\rho$, $L_1 = 738/\rho$, $L_2 = 2688/\rho$, and $L_3 = 4360/\rho$, where ρ represents rock density covering a sample in g/cm^3 (Granger and Muzikar, 2001). Density of overlying mass in the catchment during erosion is assumed to be 2.6 g/cm^3, and the bulk density of sediment in the PCC is assumed to be 2.2 g/cm^3, and τ_{Al} and τ_{Be} represent the radioactive mean lives for ^{26}Al and ^{10}Be (1.02x10^6 and 1.93x10^6 yrs, respectively; Norris et al., 1983; Nishiizumi et al., 2007)

Buried sediment derived from a steadily eroding source retains a concentration of CRNs that evolves through time as a function of the pre-burial concentration (itself a function of erosion rate), and the time since burial (Granger and Muzikar, 2001):

$$(3)\ N_{Al}(t) = N_{Al}(0)\exp\left(\frac{-t}{\tau_{Al}}\right) + P_{Al}(d)\tau_{Al}[1 - \exp\left(\frac{-t}{\tau_{Al}}\right)]$$

$$(4)\ N_{Be}(t) = N_{Be}(0)\exp\left(\frac{-t}{\tau_{Be}}\right) + P_{Be}(d)\tau_{Be}[1 - \exp\left(\frac{-t}{\tau_{Be}}\right)]$$

Where $N_{Al,Be}$ is the number of atoms/g SiO_2, t is time in years, $P_{Al,Be}$ are production rates in atoms/yr/g SiO_2, and d is sample depth in cm (Chmeleff et al., 2010). In equations three and four, the first term describes post-burial radioactive decay, and the second term describes post-burial production of CRNs. At depths greater than several 10s of m, the right-hand term may be considered negligible, but post-burial production in shallowly buried sediment may be significant (Granger and Muzikar, 2001). Lacustrine environments such as pluvial lakes provide extra post-depositional shielding to sediment from cosmic rays, yet we elected to use an equation with terms that describe muonogenic post-burial CRN production:

$$(5)\ P_{Al}(d) = A_0 \exp\left(\frac{-d}{L_0}\right) + A_1 \exp\left(\frac{-d}{L_1}\right) + A_2 \exp\left(\frac{-d}{L_2}\right) + A_3 \exp\left(\frac{-d}{L_3}\right)$$

$$(6)\ P_{Be}(d) = B_0 \exp\left(\frac{-d}{L_0}\right) + B_1 \exp\left(\frac{-d}{L_1}\right) + B_2 \exp\left(\frac{-d}{L_2}\right) + B_3 \exp\left(\frac{-d}{L_3}\right)$$

where A and B are mechanisms of CRN production as given in equations one and two. Equations one through six combine through substitution to form a system of two equations and two unknowns, time (t) and erosion rate (E), and using measured CRN concentrations ($N_{Al,Be}$) and the depth of each sample (d), we may solve for both t and E. To recover t and E, we forward model pre-burial concentrations of CRNs, and use a least-squares optimization to determine a best-fit burial age and denudation rate for each measured pair of CRN concentrations (after Craddock et al., 2010). We used published sea-level high latitude reference production rates for ^{26}Al and ^{10}Be of 28.5 and 4 atoms/g SiO_2/yr, respectively (Borchers et al., 2016), and scaled them to the catchment average production rates using latitude and catchment hypsometry to correct for altitude and shielding by the horizon, resulting in catchment average production rates for ^{26}Al and ^{10}Be of 102 and 14.3 atoms/yr/g SiO_2, respectively (Stone, 2000; and code described in Dortch et al., 2011).

3.4 Assumptions Associated with Burial Age and Paleodenudation Rate Calculations

To calculate the $^{26}Al/^{10}Be$ burial age and paleodenudation rate from sediment in the PCC we assumed the sampled bed was instantaneously buried to the modern depth below the fan surface (~500 m asl). In reality, deposits aggraded by accumulation on the alluvial-fan surface and rapid tectonically controlled subsidence of the hanging wall. A conservative estimate for the average aggradation rate in the PCC is at least ~100 – 400 m/Ma (Vogel et al., 2002). Craddock et al. (2010) calculated burial ages and denudation rates using an instantaneous emplacement model, and again using a depth-dependent model; they found calculating burial ages and denudation rates using the instantaneous emplacement model only resulted in significant bias when aggradation rates were very low, on the order of 10 m/Ma, which is an order of magnitude lower than our lowest estimate of aggradation rate.

We assumed a uniform distribution of quartz-bearing lithology in the catchment, and we made no corrections for recent exposure to cosmic rays during exhumation, because (1) we have no way to constrain the timing and rate of headward erosion in the PCC, except that incision occurred after deposition of the youngest strata, and (2) we feel the measures taken during sampling, as outlined in section 3.2, ensure samples were relatively well-shielded from modern exposure. Reported errors for burial ages and denudation rates were calculated using the analytical uncertainties (Craddock et al., 2010; Oskin et al., 2017).

4.0 RESULTS

4.1 Depositional Lithofacies Associations of the Pleasant Canyon Complex

We used data from measured lithostratigraphic sections to construct depositional lithofacies and lithofacies associations for stratigraphic units in the PCC (after Blair and Mcpherson, 2008). Example lithofacies and lithofacies associations are pictured in Figure 4, and the large-scale stacking patterns of facies associations are presented in Figure 5 (See Supplementary material S2 for complete description).

Lithofacies of the PCC fall under one of two broad groups of depositional environments, those deposited in or modified by subaqueous lacustrine environments during pluvial intervals termed the Lacustrine Lithofacies Association, or those deposited on a subaerial alluvial fan surface termed the Alluvial Lithofacies Association (after Blair and McPherson, 2008). In addition, we note the occurrence of both Lacustrine and Alluvial Lithofacies in close vertical association, which we call a Mixed Lithofacies Association.

4.1.1 Lacustrine (and Mixed) Lithofacies Association

The Lacustrine Lithofacies Association (Fig. 4c – l) is defined by laterally continuous grey- to white-colored, finely laminated to featureless beds of clay, silt, and sand. In Section One, several meters of rhythmically bedded sandy turbidites are preserved (Fig. 4h). Characteristic lithofacies that define the Lacustrine (and Mixed) Lithofacies Association include Lithofacies F: Fine silt to clay (Fig. 4c – 4i), Lithofacies Gcr: rounded, clast-supported gravel conglomerate (not pictured), and Lithofacies Sc: horizontally laminated and contorted sand beds (Fig. 4h).

The 'mixed' aspect of this lithofacies association refers to lithofacies (Fig. 4a, b, & l) that are interpreted as distinct environments of deposition, alluvial and lacustrine, which are stacked in close vertical succession, thus representing a mixed association. Where fine-grained units interpreted as lacustrine (F, Sl) are interbedded with sands (Sl, Sg), and coarse-grained gravel conglomerates (Gc, Gm), we interpret a shallow or ephemeral lake with rapidly fluctuating water level or environment of deposition (examples pictured in Figure 4a, 4b, and in the upper 1/3 of Figure 4k, and 4i).

4.1.2 Alluvial Lithofacies Association

Alluvial fan facies are ubiquitous within the PCC, and are like those described in numerous publications (*e.g.* Blair and McPherson, 2008). In the PCC, these facies are composed primarily of cobble to boulder conglomerates interbedded with thin (cm) to thick (m) clean to muddy sand beds of varying but typically low lateral continuity (Fig. 4m, n). Characteristic lithofacies that define the Alluvial Lithofacies Association include Lithofacies Gm: matrix-supported gravel conglomerate (Fig. 4m, n), Lithofacies Gc: clast-supported gravel conglomerate (Fig. 4m), Lithofacies Sg: Granule-pebble rich sand (Fig. 4a), Lithofacies Sh: horizontally laminated or featureless sand (Fig. 4a, d, h).

4.2 Stratigraphic Architecture and Depositional Evolution of the PCC

Here we use our scheme of lithofacies associations, and documented large-scale stratigraphic architecture to describe the overall depositional history of the PCC (Fig. 5). Basal deposits of the PCC indicate early deposition was dominated by coarse grained, muddy debris flows, most likely on an alluvial fan surface, separated by laterally discontinuous and patchy lacustrine-influenced conglomerate (minor lacustrine lithofacies; Gcr, Gc), as evidenced by clast rounding, open framework, and relatively coarse matrix content.

Stratigraphically above the basal alluvial-fan dominated component of the PCC, the sedimentological record shows a significant episode of system flooding, lake deepening, and backstepping of coarse-grained lithofacies (positioned at ~115 – 120 m above base of Section

Two, and ~19 – 30 m above base of section one). The Lacustrine Lithofacies Association at this interval (lithofacies F, and Sl) signals the greatest relative water depth, and likely a major full glacial-pluvial climate event. Preservation of sandy sediment gravity flows and meters of finely laminated silt to clay beds attest to deeper lake conditions during this phase of PCC evolution.

Overlying the Lacustrine Lithofacies Association, we document a transition from dominantly fine-grained deposits to thin sands, granule to pebbly sands, and muddy alluvial sediments that prograde across fine grained facies, and grade laterally in the dip direction into lacustrine facies. The mixed association of both alluvial and lacustrine lithofacies (Sl, Sg) grades vertically into coarsening upward bundles of sand, pebble, and cobble to boulder conglomerate (Sl, Sg, Gm, Gc). This evolution is likely in response to changes in base level associated with lake desiccation.

Due to lateral discontinuity of individual beds of alluvial lithofacies, we used the prominent lacustrine unit in the upper portion of the outcrop transect (Fig.5) to correlate the two measured sections and to create a composite stratigraphic section for the PCC. We note syndepositional normal faulting in the south part of the PCC, and subtle depositional geometry of the paleo fan may explain the overall thickening, and lower stratigraphic position of the lacustrine unit in Section One (See Supplementary Fig. 2.2).

4.3 CRN-derived Stratigraphic Ages and Paleodenudation Rates

Table 1 shows results of blank corrected AMS measurements, $^{26}Al/^{10}Be$ burial ages, and paleodenudation rates for samples from the PCC and modern catchment outlets. Figure 6 shows the global $\delta^{18}O$ curve (Lisiecki and Raymo, 2005) plotted with a synthesis of our stratigraphic and CRN-derived data sets, including a composite stratigraphic section with sample locations, interpreted lithofacies associations, CRN-derived burial ages, and CRN-derived paleodenudation rates plotted against composite stratigraphic thickness.

The results of burial dating in the PCC yield a depositional age model that supports previous interpretations for the age of basal stratigraphy of at least ca. 0.9 Ma (ca. 20 m above playa floor; Vogel et al., 2002). However, our results indicate that the deposit was actively aggrading in a proximal alluvial fan environment as early as ca. 1.55 ± 0.16 Ma (Fig. 6). A basal burial ages of ca. 1.55 ± 0.16 Ma, and a stratigraphically higher sample age of 1.16 ± 0.20 Ma obey stratigraphic superposition, and samples generally become younger up-section. Stratigraphically highest ^{26}Al/^{10}Be burial ages are ca. 0.52 ± 0.18 Ma, 0.36 ± 0.16 Ma, 0.33 ± 0.14 Ma, and 0.65 ± 0.22 Ma (Table 1 & Fig. 6).

Samples of modern sediment from Pleasant Canyon and Middle Park Canyon outlets yield denudation rates of 24 ± 1 mm/kyr and 28 ± 2 mm/kyr, respectively, averaged over ca. 21 – 25 kyr timescales. Paleodenudation rates derived from Pleistocene PCC outcrop samples vary from 28 ± 5 mm/kyr up to 54 ± 7 mm/kyr, with a long term mean denudation rate for the PCC of 36 ± 8 mm/kyr (1σ for all PCC CRN-derived denudation rates; see Table 1).

The highest measured rate, 54 mm/kyr, represents a >2x increase compared to the modern, and lowest, rate of 24 mm/kyr for Pleasant Canyon. Individual paleodenudation rates have uncertainties that do not overlap, and three samples (21% of samples) have rates that fall outside an envelope defined by the mean and standard deviation of all PCC samples (36 ± 8 mm/kyr; 1σ). Several samples do have errors that do not overlap, but are within one standard deviation of the mean rate. We note that the highest magnitudes of paleodenudation rates are observed in samples below and above the major lacustrine interval preserved within the PCC (Fig. 6). Overall, the highest and lowest CRN-derived denudation rates vary by +50%/-33% from the long-term mean rate, and 20% of the samples from alluvial fan stratigraphy record a departure from the long-term mean paleodenudation rate.

5.0 DISCUSSION

5.1 Climate-driven Variability in Catchment-fan System Response

Our primary objective was to explore how climate transitions affect the magnitudes and temporal variability of CRN-derived signals of catchment denudation and sediment flux in a natural unglaciated system. We documented the stratigraphic evolution of the depositional segment of the PCC, which records sediment flux and glacial-pluvial events in Panamint valley, and used CRN-derived paleodenudation rates as a proxy for catchment-fan sediment fluxes through time. Though CRN-derived paleodenudation rates for the PCC were similar in magnitude for much of >1 Myr interval, these rates were not constant. In the PCC, the long-term CRN-derived paleodenudation rate (36 ± 8 mm/kyr, between ca. 1.5 Ma through ca. 0.3 or 0.6 Ma) includes samples with higher calculated rates (49 and 54 mm/kyr). Modern CRN-derived denudation rates from Pleasant and Middle Park Canyons are systematically lower than all but one paleodenudation rate from the PCC (Table 1), suggesting Holocene denudation rates are anomalously low, or potentially that hillslope and fluvial sediment transport processes during the Holocene differ from those responsible for deposition on the active paleo-fan surface.

Taken at face value, the CRN-derived paleodenudation rates preserved in alluvial fan stratigraphy have varied by at least a factor of ~2x. A pattern of relatively steady paleodenudation rates juxtaposed with significant variability in the high end as measured in the PCC, is similar to the pattern of imposed erosion rate vs. resulting CRN-derived erosion rate simulated in Figure 1c. Our integrated stratigraphic framework documenting the presence of significant lacustrine facies in the PCC suggests denudation rate and sediment supply were variable some time before and after a major pluvial lake highstand preserved in the upper PCC (Fig. 6c – e). This qualitative comparison between our empirical record and a predicted pattern of actual erosion vs. CRN-derived erosion, and the presence of stratigraphic evidence for major climate transitions in Panamint Valley associated with variability in CRN-derived denudation/sediment flux, suggests that glacial-interglacial climate has an observable effect on CRN-derived denudation rates in unglaciated catchment-fan systems.

Our study documents a great degree of variability in both depositional environments, and CRN-derived apparent paleodenudation rates measured in alluvial fan strata deposited after the middle-Pleistocene transition. Thus, a plausible interpretation of our data—and a potential explanation for other studies that have not documented variability across climate transitions—is that 100 kyr periods may be more effective than 40 kyr periods at modulating CRN concentrations in sediment exiting catchments.

We cannot rule out similar CRN-derived denudation rate variability in the lower portion of the PCC, but we may compare the record from the PCC to other CRN-derived paleodenudation records measured across climate transitions in unglaciated catchments. Although climate cooling and increased variability across the middle Pleistocene transition did not affect CRN-derived paleodenudation rates (Oskin et al., 2017; Granger et al., 2001), post-middle-Pleistocene CRN-derived paleodenudation rates from Fisher Valley, Utah, between ca. 0.7 – 0.6 Ma, varied by as much as 2x, and are up to 2x higher than the modern (Holocene) rates (Balco and Stone, 2005). Periglacial processes are shown to increase CRN-derived denudation during the last glacial maximum compared to the Holocene (Marshall et al., 2015). A related hypothesis is that longer periods of climate extremes and subsequent transitions in a post middle

Pleistocene world (Fig. 6b; Lisieki and Raymo, 2005) conceivably lead to changes to processes regimes that produce measurable variability in CRN concentrations (*e.g.* Garcin, et al., 2017).

In the following discussion sections, we outline important limitations to the interpretation of CRN-derived empirical data sets, and present a first-order analysis of alternative drivers of observed variability in apparent paleodenudation rates.

5.2 Limitations to Interpretation of CRN-derived Signals from Alluvial Fan Stratigraphy

Changes in measured CRN-derived denudation and sediment supply apparent in our record allude to catchment response to climate change. However, we acknowledge that several limitations of the CRN methodology pose challenges to assessing the true magnitude and variability of paleodenudation/sediment flux signals emitted from Pleasant Canyon. First, we note that alluvial fans may experience allogenic or autogenic driven erosion-deposition processes, introducing potential stratigraphic incompleteness and/or preferential stratal preservation (Armitage et al., 2011; D'Arcy et al., 2016; Straub and Esposito, 2013). A second challenge relates to theoretical constraints on the CRN technique. True denudation rates may only be measured using CRNs where steady state between catchment erosion and CRN flux has been reached (Bierman and Steig, 1996). In the context of Milankovitch climate forcing, a catchment's CRN export may never equilibrate to the true denudation rate/sediment flux, especially during punctuated climate events (See Fig. 1, part c). As a result, CRN-derived denudation signals extracted from alluvial stratigraphy may be smoothed compared to actual denudation/sediment flux. Last, it is plausible that the resolution of sampling for this study does not capture other periods of high or low paleodenudation/sediment supply that were recorded in alluvial stratigraphy (as in the lower portion of the PCC, *e.g.* Fig. 6).

Potential stratigraphic incompleteness, long CRN lag times, and sample resolution limit interpretations of our data set. However, normal-fault bound, rapidly subsiding alluvial basins likely represent the most complete archives of past continental surface dynamics (Straub and Esposito, 2013) highlighting the value of this data set. Furthermore, long CRN lag times may suggest that our highest CRN-derived rates actually represent minimum estimates for true denudation rates and sediment fluxes. We propose that future studies utilizing valuable alluvial fan records should consider potential stratigraphic completeness and sample resolution as first order controls on robust data interpretation.

5.3 Unsteady Catchment Processes and Denudation Signal vs. Noise

Here, we also consider the potential for noise in the record, which we define as variability driven by up-system non-equilibrium processes, *e.g.* complex sediment storage and remobilization or mass wasting in the catchment. We consider two end-member scenarios: (1) thin (several m thick) and relatively old (>15 – 20 kyr since bedrock denudation) deposits stored within the upper catchment acquire a large post-erosion CRN concentration, and when remobilized, become mixed with sediment of average concentration, resulting in depressed apparent denudation rates, and (2) localized mass wasting within the catchment supplies sediment with relatively low CRN concentrations, which when mixed with sediment of average CRN concentration, results in an increase of apparent paleodenudation rate. We prescribed plausible CRN concentrations to sediment from each scenario—stored sediment or landslide-derived sediment—and applied a simple two end-member mixing model to estimate the relative contribution from each source necessary to drive variability equal to the highest and lowest

CRN-derived denudation rates from the PCC (See Supplementary material S3 for complete explanation).

Figure 7 shows the results of mixing high- and low-concentration sediment with average concentration sediment. This analysis suggests that our lowest denudation rate from the PCC (24 mm/kyr) requires ~48% of sediment to be derived from a high-concentration, old deposit, whereas the highest calculated paleodenudation rate from the PCC (54 mm/kyr), requires ~56% of sediment to be derived from a low-concentration source, presumably representing landslide-derived material in this framework.

We observe no evidence in the upper catchment of significant fluvial incision and terrace development that might be expected for >10^4 yr old deposits. The implication is that the first scenario with mixing of significant amounts of old stored sediment (at least 48%) is unlikely for samples from the PCC. In the case of the second scenario, mixing of large proportions (~56%) of mass-wasting derived sediment is difficult to evaluate; it may be plausible given the high-relief and short length-scale of the system, which suggests variability in the high end could be driven by mass wasting. Similar proportions (~50%) of landslide-derived sediment were deduced from ^{10}Be concentrations found in some fluvial systems after widespread coseismic landslides associated with the 2008 Wenchuan earthquake (West et al., 2014). Yet another possibility is that climate and mass wasting are linked, and the observed CRN-derived paleodenudation variability was driven by mass wasting events brought on by climate transitions. The questions of whether climate forcing and erosion were in phase or not, and whether CRN concentrations in the PCC are the result of steady or stochastic events remains unresolved. However, the lack of significant evidence for sediment storage and major landslides in the catchment, and the association of high CRN-derived paleodenudation rates with documented stratigraphic response to changing climate, *e.g*. lacustrine strata of glacial-pluvial origin in the PCC (Fig. 6), are lines of evidence consistent with climate transitions driving variability in CRN concentrations and sediment fluxes from catchment to fan.

6.0 CONCLUSIONS

We measured cosmogenic radionuclides (CRNs; ^{26}Al and ^{10}Be; n = 13 samples) vertically through a succession of outcropping Pleistocene alluvium, and in modern sediment (n = 2 samples) from a linked catchment-fan system to examine the effects of climate change on CRN-derived catchment denudation rates and source-to-sink sediment transfer. Many of the resultant paleodenudation measurements from the Pleasant Canyon complex (PCC) are remarkably similar in magnitude over the period of interest (ca. 1.5 Ma through ca. 0.3 – 0.6 Ma), with a mean rate of 36 ± 8 mm/kyr (1σ). However, paleodenudation and modern denudation rates do display maximum variability of +50%/-33% from the mean long-term rate. Full glacial climate in the Panamint Valley region was on average 5 – 6 °C colder, and ~50 – 100% wetter (D'Arcy et al., 2016), conditions that resulted in major pluvial lake formation in Panamint Valley as deduced from lacustrine strata preserved in the PCC. Simulated CRN lag times suggest that the highest measured CRN-derived paleodenudation rates (49 – 54 mm/kyr) from the PCC may represent minimum estimates of true catchment denudation and sediment flux. We explored other potential drivers of denudation variability, specifically sediment supplied from localized landslides in the catchment. An end-member mixing model suggests that more than 50% of low-CRN-concentration landslide-derived sediment would be required to produce the highest denudation rates in our record. Sample age resolution prevents us from delineating specific relationships between paleodenudation magnitude and specific Milankovitch cycles, but documented lithofacies associations preserved in the PCC depositional segment suggest the highest CRN-derived paleodenudation occurs in stratigraphic association with climatic transitions, *i.e.,* from lacustrine to alluvial lithofacies. High CRN-derived paleodenudation rates were recovered from samples deposited after the middle Pleistocene transition—the change from 40 to 100 kyr periods—suggesting that 100 kyr periodicity in climate forcing may result in significant changes in erosion rates, and thus CRN concentrations within this, and probably other steep, arid, unglaciated catchment-fan systems globally.

ACKNOWLEDGEMENTS

Financial support was provided by an American Chemical Society-Petroleum Research Fund-Doctoral New Investigator grant (#53553-DNI8) to BWR with additional analytical support from a Seed Grant from the Purdue Rare Isotope Measurement Laboratory (PRIME Lab) to CM and BWR. Two anonymous reviewers provided insightful and helpful reviews that significantly improved the quality of this manuscript. James Spotila, William Craddock, and Andrew Cyr provided helpful conversations and insightful feedback during the evolution of this work. Marek Cichanski provided insight on the provenance of sediment in the PCC. Neal Auchter and Theodore Them assisted with field work, and others from the Virginia Tech Sedimentary Systems Research Group offered constructive feedback. BWR thanks Hannah Scherer for assistance in the field during project inception. Ron Schott photographed the Pleasant Canyon complex in beautiful detail (Figure 2). Gigapans may be found at: http://www.gigageology.org/Collections/PanamintValley.html

APPENDICIES

Supplementary material related to this article may be found online at…

REFERNCES

Albee, A.L., Labotka, T.C., Lanphere, M.A., McDowell, S.D., 1981. Geologic Map of the Telescope Peak Quadrangle, California.

Allen, P.A., 2008. Time scales of tectonic landscapes and their sediment routing systems. Geol. Soc. London, Spec. Publ. 296, 7–28. doi:10.1144/SP296.2

Allen, P.A., Densmore, A.L., 2000. Sediment flux from an uplifting fault block. Basin Res. 12, 367–380. doi:10.1046/j.1365-2117.2000.00135.x

Armitage, J.J., Duller, R. a., Whittaker, A.C., Allen, P. A., 2011. Transformation of tectonic and climatic signals from source to sedimentary archive. Nat. Geosci. 4, 231–235. doi:10.1038/ngeo1087

Balco, G., Stone, J.O.H., 2005. Measuring middle Pleistocene erosion rates with cosmic-ray-produced nuclides in buried alluvial sediment, Fisher Valley, southeastern Utah. Earth Surf. Process. Landforms 30, 1051–1067. doi:10.1002/esp.1262

Bidgoli, T.S., Amir, E., Walker, J.D., Stockli, D.F., Andrew, J.E., Caskey, S.J., 2015. Low-temperature thermochronology of the Black and Panamint mountains, Death Valley, California: Implications for geodynamic controls on Cenozoic intraplate strain. Lithosphere 7, 473–480. doi:10.1130/L406.1

Bierman, P., Steig, E.J., 1996. Estimating Rates of Denudation Using Cosmogenic Isotope Abundances in Sediment. Earth Surf. Process. Landforms 21, 125–139. doi:10.1002/(SICI)1096-9837(199602)21:2<125::AID-ESP511>3.0.CO;2-8

Blair, T.C., Mcpherson, J.G., 2008. Quaternary sedimentology of the Rose Creek fan delta, Walker Lake, Nevada, USA, and implications to fan-delta facies models. Sedimentology 55, 579–615. doi:10.1111/j.1365-3091.2007.00913.x

Borchers, B., Marrero, S., Balco, G., Caffee, M., Goehring, B., Lifton, N., Nishiizumi, K., Phillips, F., Schaefer, J., Stone, J., 2016. Geological calibration of spallation production rates in the CRONUS-Earth project. Quat. Geochronol. 31, 188–198. doi:10.1016/j.quageo.2015.01.009

Castelltort, S., Van Den Driessche, J., 2003. How plausible are high-frequency sediment supply-driven cycles in the stratigraphic record? Sediment. Geol. 157, 3–13. doi:10.1016/S0037-0738(03)00066-6

Chmeleff, J., von Blanckenburg, F., Kossert, K., Jakob, D., 2010. Determination of the ^{10}Be half-life by multicollector ICP-MS and liquid scintillation counting. Nucl. Instruments Methods Phys. Res. Sect. B Beam Interact. with Mater. Atoms 268, 192–199. doi:10.1016/j.nimb.2009.09.012

Cichanski, M., 2000. Low-angle, range-flank faults in the Panamint, Inyo, and Slate ranges, California: Implications for recent tectonics of the Death Valley region. Bull. Geol. Soc. Am. 112, 871–883. doi:10.1130/0016-7606(2000)112<871:LRFITP>2.0.CO;2

Covault, J.A., Romans, B.W., Graham, S.A., Fildani, A., and Hilley, G.E., 2011. Terrestrial source to deep-sea sink sediment budgets at high and low sea levels: insights from tectonically active southern California. Geology 39:619–622.

Craddock, W.H., Kirby, E., Harkins, N.W., Zhang, H., Shi, X., Liu, J., 2010. Rapid fluvial incision along the Yellow River during headward basin integration. Nat. Geosci. 3, 209–213. doi:10.1038/ngeo777

D'Arcy, M., Whittaker, A.C., Roda-Boluda, D.C., 2016. Measuring alluvial fan sensitivity to past climate changes using a self-similarity approach to grain-size fining, Death Valley, California. Int. Assoc. Sedimentol. Spec. Publ. doi:10.1111/sed.12308

Densmore, A.L., Anderson, R.S., 1997. Tectonic geomorphology of the Ash Hill fault, Panamint Valley, California. Basin Res. 9, 53–63. doi:10.1046/j.1365-2117.1997.00028.x

Densmore, A.L., Gupta, S., Allen, P.A., Dawers, N.H., 2007. Transient landscapes at fault tips. J. Geophys. Res.: Earth Surface 112, F03S08. doi:10.1029/2006JF000560

Dortch, J.M., Owen, L.A., Schoenbohm, L.M., Caffee, M.W., 2011. Asymmetrical erosion and morphological development of the central Ladakh Range, northern India. Geomorphology 135, 167–180. doi:10.1016/j.geomorph.2011.08.014

Frankel, K.L., Brantley, K.S., Dolan, J.F., Finkel, R.C., Klinger, R.E., Knott, J.R., Machette, M.N., Owen, L.A., Phillips, F.M., Slate, J.L., Wernicke, B.P., 2007. Cosmogenic ^{10}Be and ^{36}Cl geochronology of offset alluvial fans along the northern Death Valley fault zone: Implications for transient strain in the eastern California shear zone. J. Geophys. Res. Solid Earth 112, 1–18. doi:10.1029/2006JB004350

Garcin, Y., Schildgen, T.F., Torres Acosta, V., Melnick, D., Guillemoteau, J., Willenbring, J., Strecker, M.R., 2017. Short-lived increase in erosion during the African Humid Period: Evidence from the northern Kenya Rift. Earth Planet. Sci. Lett. 459, 58–69. doi:10.1016/j.epsl.2016.11.017

Glotzbach, C., Van Der Beek, P., Carcaillet, J., Delunel, R., 2013. Deciphering the driving forces of erosion rates on millennial to million-year timescales in glacially impacted landscapes: An example from the Western Alps. J. Geophys. Res. Earth Surf. 118, 1491–1515. doi:10.1002/jgrf.20107

Granger, D.E., Fabel, D., Palmer, A.N., 2001. Pliocene - Pleistocene incision of the Green River, Kentucky, determined from radioactive decay of cosmogenic 26Al and10Be in Mammoth Cave sediments. Bull. Geol. Soc. Am. 113, 825–836. doi:10.1130/0016-7606(2001)113<0825:PPIOTG>2.0.CO;2

Granger, D.E., Muzikar, P.F., 2001. Dating sediment burial with in situ-produced cosmogenic nuclides: Theory, techniques, and limitations. Earth Planet. Sci. Lett. 188, 269–281. doi:10.1016/S0012-821X(01)00309-0

Granger, D.E., Schaller, M., 2014. Cosmogenic Nuclides and Erosion at the Watershed Scale. Elements 10, 369–373. doi:10.2113/gselements.10.5.369

Gulick, S.P.S., Jaeger, J.M., Mix, A.C., Asahi, H., Bahlburg, H., Belanger, C.L., Berbel, G.B.B., Childress, L., Cowan, E., Drab, L., Forwick, M., Fukumura, A., Ge, S., Gupta, S., Kioka, A., Konno, S., LeVay, L.J., März, C., Matsuzaki, K.M., McClymont, E.L., Moy, C., Müller, J., Nakamura, A., Ojima, T., Ribeiro, F.R., Ridgway, K.D., Romero, O.E., Slagle, A.L., Stoner, J.S., St-Onge, G., Suto, I., Walczak, M.D., Worthington, L.L., Bailey, I., Enkelmann, E., Reece, R., Swartz, J.M., 2015. Mid-Pleistocene climate transition drives net mass loss from rapidly uplifting St. Elias Mountains, Alaska. Proc. Natl. Acad. Sci. 1–6. doi:10.1073/pnas.1512549112

Hidy, A.J., Gosse, J.C., Blum, M.D., Gibling, M.R., 2014. Glacial–interglacial variation in denudation rates from interior Texas, USA, established with cosmogenic nuclides. Earth Planet. Sci. Lett. 390, 209–221. doi:10.1016/j.epsl.2014.01.011

Jannik, N.O., Phillips, F.M., Smith, G.I., Elmore, D., 1991. A ^{36}Cl chronology of lacustrine sedimentation in the Pleistocene Owens River system. Geol. Soc. Am. Bull. 103, 1146–1159. doi:10.1130/0016-7606(1991)103<1146:ACCOLS>2.3.CO;2

Jayko, A.S., 2005. Late Quaternary denudation, Death and Panamint Valleys, eastern California. Earth-Science Rev. 73, 271–289. doi:10.1016/j.earscirev.2005.04.009

Jerolmack, D.J., Paola, C., 2010. Shredding of environmental signals by sediment transport. Geophys. Res. Lett. 37, 1–5. doi:10.1029/2010GL044638

Lal, D., 1991. Cosmic ray labeling of erosion surfaces: in situ nuclide production rates and erosion models. Earth Planet. Sci. Lett. 104, 424–439. doi:10.1016/0012-821X(91)90220-C

Marshall, J.A., Roering, J.J., Bartlein, P.J., Gavin, D.G., Granger, D.E., Rempel, A.W., Praskievicz, S.J., Hales, T.C., 2015. Frost for the trees: Did climate increase erosion in unglaciated landscapes during the late Pleistocene? Sci. Adv. 1, e1500715–e1500715. doi:10.1126/sciadv.1500715

Mason, C.C., Fildani, A., Gerber, T., Blum, M.D., Clark, J.D., Dykstra, M., 2017. Climatic and anthropogenic influences on sediment mixing in the Mississippi source-to-sink system using detrital zircons: Late Pleistocene to recent. Earth Planet. Sci. Lett. 466, 70–79. doi:10.1016/j.epsl.2017.03.001

Nishiizumi, K., Imamura, M., Caffee, M.W., Southon, J.R., Finkel, R.C., McAninch, J., 2007. Absolute calibration of ^{10}Be AMS standards. Nucl. Instruments Methods Phys. Res. Sect. B Beam Interact. with Mater. Atoms 258, 403–413. doi:10.1016/j.nimb.2007.01.297

Norris, T.L., Gancarz, A.J., Rokop, D.J., Thomas, K.W., 1983. Half-life of 26Al. J. Geophys. Res.: Solid Earth 88, B331. doi:10.1029/JB088iS01p0B331

Oskin, M.E., Longinotti, N.E., Peryam, T., Dorsey, B., DeBoer, C., Housen, B., Blisniuk, K., 2017. Steady ^{10}Be-derived paleo-erosion rates across the Plio-Pleistocene climate transition, Fish Creek-Vallecito basin, California. J. Geophys. Res. Earth Surf. doi:10.1002/2016JF004113

Oster, J.L., Ibarra, D.E., Winnick, M.J., Maher, K., 2015. Steering of westerly storms over western North America at the Last Glacial Maximum. Nat. Geosci. 8, 201–205. doi:10.1038/ngeo2365

Oswald, J.A., Wesnousky, S.G., 2002. Neotectonics and quaternary geology of the Hunter Mountain fault zone and Saline Valley region, Southeastern California. Geomorphology 42, 255–278. doi:10.1016/S0169-555X(01)00089-7

Paola, C., Heller, P.L., Angevine, C.L., 1992. The large scale dynamics of grain size variation in alluvial basins, 1: Theory. Basin Res. doi:10.1111/j.1365-2117.1992.tb00145.x

Phillips, F.M., 2008. Geological and hydrological history of the paleo – Owens River drainage since the late Miocene, Geological Soc. of America Special Publications 2439, 1–36. doi:10.1130/2008.2439(06).

Puchol, N., Charreau, J., Blard, P.H., Lavé, J., Dominguez, S., Pik, R., Saint-Carlier, D., Team, A., 2017. Limited impact of quaternary glaciations on denudation rates in central Asia. Bull. Geol. Soc. Am. 129, 479–499. doi:10.1130/B31475.1

Lisiecki, L.E., Raymo, M.E., 2005. A Pliocene-Pleistocene stack of 57 globally distributed benthic δ 18O records. Paleoceanography 20, 1–17. doi:10.1029/2004PA001071

Romans, B.W., Castelltort, S., Covault, J.A., Fildani, A., Walsh, J.P., 2016. Environmental signal propagation in sedimentary systems across timescales. Earth-Science Rev. 153, 7–29. doi:10.1016/j.earscirev.2015.07.012

Smith, R.S.U., 1976. Late Quaternary Pluvial and Tectonic History of Panamint Valley, Inyo and San Bernardino Coutnies, California. California Institute of Technology.

Snyder, N.P., Hodges, K. V., 2000. Depositional and tectonic evolution of a supradetachment basin: 40Ar/39Ar geochronology of the Nova Formation, Panamint Range, California. Basin Res. 12, 19–30. doi:10.1046/j.1365-2117.2000.00108.x

Stock, G.M., Anderson, R.S., Finkel, R.C., 2005. Rates of erosion and topographic evolution of the Sierra Nevada, California, inferred from cosmogenic ^{26}Al and ^{10}Be concentrations. Earth Surf. Process. Landforms 30, 985–1006. doi:10.1002/esp.1258

Stone, J.O., 2000. Air pressure and cosmogenic isotope production. J. Geophys. Res. Solid Earth 105, 23753–23759. doi:10.1029/2000JB900181

Straub, K.M., Esposito, C., 2014. Influence of Water and Sediment Supply on the Completeness of the Stratigraphic Record and the Construction of Stratigraphic Surfaces in Alluvial Fans and Deltas. Journal of Geophysical Research: Earth Surface, 118, 625–637, doi:10.1002/jgrf.20061

Vogel, M.B., Jayko, A.S., Wooden, J.L., Smith, R.S.U., 2002. Quaternary exhumation rate Central Panamint Range, California from U–Pb Zircon Ages. Abstracts with Programs, Geological Society of America 34, 249.

West, A. J., R. Hetzel, G. Li, Z. Jin, F. Zhang, R. G. Hilton, and A. L. Densmore (2014), Dilution of 10 Be in detrital quartz by earthquake-induced landslides?: Implications for determining denudation rates and potential to provide insights into landslide sediment dynamics, Earth Planet. Sci. Lett., 396, 143-153, doi:10.1016/j.epsl.2014.03.058.

FIGURE CAPTIONS

Figure 1: Modeled changes in sediment flux (q_s per unit width) and erosion rate across two timescales (Myr and kyr), resulting from perturbations in climatic or tectonic boundary conditions in a catchment-fan system bounded by a range-front normal fault, and simulated imposed erosion rate plotted with resultant CRN-derived erosion rate. Time progresses from left to right in all plots. **a**: q_s response to stepwise increase (+100%, black line) or decrease (-50%, gray line) in precipitation rate. **b**: q_s response to stepwise increase (+100%, black line) or decrease (-50%, gray line) in fault slip rate. Dashed vertical red line indicates timing of change in forcing in parts a and b. Modified from Densmore et al. (2007). **c**: Simulated response of cosmogenic radionuclide (CRN) derived erosion rates to a change in actual (imposed) erosion rate. The duration of the simulation is similar to that of middle to late Pleistocene Milankovitch periods of 100 kyrs. Green solid line represents user defined erosion rate, and blue dashed line represents the model output, or CRN-derived erosion rate through time. ^{10}Be production rate for simulation as described in main text and code described in Garcin et al. (2017).

Figure 2: Study area shaded relief map, regional paleoclimatic reconstruction, and photopanorama of the Pleasant Canyon Complex (PCC). **a**: Topography, and active faults of the Panamint/Death Valley area. Pleasant Canyon catchment-fan system highlighted in red dashed lines. Extents of Pleistocene pluvial lakes of the Owens River system highlighted in dashed blue lines, and blue arrows denote pluvial lake flow directions into and out of Panamint Valley (Reheis et al., 2014). **b**: Last glacial maximum paleoclimatic reconstruction showing precipitation change for the western United States after Oster et al. (2015). **c**: Photopanorama of the PCC with locations of measured sections (Photo credit: Ron Schott). AHFZ = Ash Hill fault

zone, Mid. Park = Middle Park Canyon, PEDF = Panamint Emigrant detachment fault, PVFZ = Panamint Valley fault zone. Fault data from U.S. Geological Survey Quaternary fault database. 1 arc second elevation data from the U.S. Geological Survey.

Figure 3: Pleasant Canyon catchment metrics. **a**: digital elevation model. **b**: Surface slope map. **c**: Areal distribution of lithology in the catchment. All units are quartz bearing except for the Sentinel Peak dolomite and probably the basalt/amphibolite unit (after Albee et al., 1981). **d:** Pleasant Canyon catchment hypsometry. Left y-axis represents total catchment area within each bin, x-axis represents elevation of catchment increasing from left to right (100 equal bins, each 22.7 m), and right y-axis is the cumulative catchment area. 1 arc second elevation data from U.S. Geological Survey.

Figure 4: Lithofacies of the Pleasant Canyon complex**. a**, **b**: Horizontally laminated and low-angle cross-stratified sand and granule- to pebble-rich beds (lithofacies Sl, Sg) that compose a gradational transition in lithofacies from Lacustrine Lithofacies Association to Alluvial Lithofacies Association. Note thick gravel debris flow capping units in **b** (lithofacies Gc, Gm). **c** – **l**: dominantly fine-grained silt and clay (lithofacies F, Sl, Sg) that composes the Lacustrine Lithofacies Association. **c**: Pebble-granule-rich sand lithofacies (Sg). **d**: Laminated sand lithofacies (Sl). **e**, **f**: Fine-grained and pebble-granule rich lithofacies (Sf, Sg, and F), with small burrows or root-traces. **g**: interbedded fine-grained and granule-rich lithofacies (F, Sg). **h**: Sandy turbidites with contorted bedding (Sl). **i**: Laminated to cross-laminated sand with weakly

developed paleosol (Sl). **j**: fine grained lacustrine lithofacies (F) with possible varves. **k**: Thick exposure (note person for scale) of fine-grained lithofacies (F, Sl) composing the Lacustrine Lithofacies Association in section one. **l**: Interbedded fine-grained and gravel lithofacies (F, Gm, Gc) that compose the Lacustrine (and Mixed) Lithofacies Association in Section Two. **m**, **n**: Interbedded clast- and matrix-supported debris flow gravels with lenticular to laterally continuous sands (lithofacies Gc, Gm, Sl, Sf) typical of the Alluvial Lithofacies Association.

Figure 5: Photomosaics and large-scale lithofacies associations and stratigraphic architecture of the Pleasant Canyon Complex (PCC). **a:** Uninterpreted photomosaic of the southwest PCC. **b**: interpreted photomosaic from part a, with colored lithofacies associations. **c**: Uninterpreted photomosaic of the northwest PCC with the ghost town of Ballarat in the foreground. **d**: Interpreted panel from part c illustrating subtle inclined geometries of progradational foresets within alluvial-lacustrine lithofacies. Lacustrine units pinch-out or grade into mixed or alluvial lithofacies associations up dip.

Figure 6a: Overview of the Pleasant Canyon complex (PCC) with schematic locations of measured lithostratigraphic sections and cosmogenic radionuclide (CRN) samples. **6b** – **e**: Pleistocene paleoclimate, PCC composite stratigraphic framework, burial ages, and paleodenudation rates since ca. 1.5 Ma. **b**: Global oxygen isotope curve of Lisiecki and Raymo, (2005), with known pluvial lake events in Panamint Valley shaded blue (after Jannick et al., 1991). **c**: Composite stratigraphic section with interpreted lithofacies associations and CRN sample numbers and positions. Blue shaded boxes indicate stratigraphic position of Lacustrine Lithofacies Associations. **d**: CRN-derived burial ages vs. composite stratigraphic height, **e**: CRN-derived paleodenudation rates vs. composite stratigraphic height beginning at ca. 1500 kyr. Dashed vertical lines are mean and standard deviation (1σ) of all paleodenudation rates. Modern catchment denudation rates are plotted at 5 meters height and shown with red circles. Individual sample error bars represent the average of upper and lower bounds (1σ) on burial age-erosion rate calculations (after Craddock et al., 2010). Refer to text and Supplementary Materials for explanation of composite stratigraphic framework.

Figure 7: Binary mixing model results. Curves represent synthetic ^{10}Be-derived denudation rates associated with a given mixture of either high CRN-concentration stored/recycled sediment (blue curve) or low CRN-concentration landslide-derived sediment (red curve), with 'average' sediment that experienced a mean erosion rate of ~36 mm/kyr.

Table 1: AMS results, ^{26}Al and ^{10}Be burial ages and denudation rates for samples from the Pleasant Canyon Complex and modern catchment outlets, Panamint Range and Valley, USA

Sample location information						AMS Results (blank corrected)				Burial ages and denudation rates			
sample ID	lat.	lon.	elevation (m asl)	depth (cm)	location	^{26}Al (a/g SiO_2)	*error	^{10}Be (a/g SiO_2)	error	$^{26}Al/^{10}Be$ burial age (yr)	error (yr)	denudation rate (mm/kyr)	error (mm/kyr)
PAN01	36.02861	-117.21487	430	7000	PCC	1309759	43805	252927	6311	705,000	124,500	28	5
PAN02	36.0293	-117.21377	466	3400	PCC	1564624	55644	263806	9493	425,000	158,000	31	7
PAN03	36.0293	-117.21377	466	3400	PCC	1564426	77465	262072	7548	410,000	173,500	31	3.5
PAN04	36.02942	-117.21354	476	2400	PCC	1103834	40630	177904	5627	359,000	159,500	49	5
PAN05	36.0295	-117.21344	481	1900	PCC	1214501	48460	209390	6973	518,000	177,500	39	4
PAN06	36.02905	-117.21461	435	6500	PCC	1258579	64415	218528	7525	486,000	184,000	36	4.5
PAN07	36.03671	-117.21848	482	1800	PCC	1600021	59776	256047	6211	326,000	143,500	34	3
PAN08	36.03579	-117.21942	452	4800	PCC	1046392	51235	195296	5617	654,000	170,500	37	4.5
PAN09	36.03536	-117.22203	366	13400	PCC	671949	33194	160023	7205	1,164,000	201,500	34	5
PAN10	36.04724	-117.21092	412	…	Modern Pleasant Canyon	2225616	77950	362733	8772	…	…	24	0.56
PAN11	36.03868	-117.2192	482	1800	PCC	1341444	57291	245223	11679	645,000	219,500	31	4.5
PAN12	36.02749	-117.21577	390	…	Modern Middle Park	1637336	65025	287452	16818	…	…	28	1.6
PAN13	36.03493	-117.21848	448	5200	PCC	755308	29065	137675	6190	618,000	184,000	54	7.5
PAN14	36.02861	-117.21487	430	7000	PCC	1210537	60013	215151	8287	536,000	188,500	36	5
PAN15	36.04103	-117.22286	336	16400	PCC	471472	20247	134163	4084	1,549,000	156,000	34	4

*All errors based on one standard deviation of analytical uncertainties

SUPPLEMENTARY MATERIALS

Supplementary Text S1.0, S2.0, S3.0, References

Supplementary Figures S1, S2.1, S2.2, S3

Supplementary Table 1 AMS results

S1.0 CLAST PROVENANCE OF THE PLEASANT CANYON COMPLEX

Sediments preserved in deposits of the PCC were mainly derived from the Pleasant Canyon catchment, as indicated by the position of the deposit at the canyon mouth, the progradation direction of the PCC, a closed drainage in the upper portions of Middle Park catchment, and sediment provenance (clast compositions) in measured sections. Pleasant Canyon contains a unique geologic unit known as the World Beater complex, a foliated gneiss with well-developed augen porphyroblasts (Albee et al., 1981). The World Beater is not present in the Middle Park catchment; thus, the presence of World Beater clasts supports a model where sediment preserved in the PCC was derived largely from the Pleasant Canyon. We conducted reconnaissance-level field work to survey for the presence of this unique lithology in our measured lithostratigraphic sections; clasts of World Beater were ubiquitous at all levels of strata in outcrop, and in float along canyon floors, (Supplementary Figure 1). We are confident that sediment in the PCC was derived from Pleasant Canyon, and that the use of a catchment average production rate derived from the hypsometry of Pleasant Canyon is justified. We note Middle Park catchment probably contributed minor amounts of sediment to the PCC, but the small difference in catchment hypsometry only affects the production of CRNs to a minor degree (~1 atom/g SiO_2/yr) and thus we elect to use one catchment production rate for all rate and age calculations for samples from outcrop in the PCC.

S2.0 DEPOSITIONAL LITHOFACIES OF THE PLEASANT CANYON COMPLEX

We used data from measured lithostratigraphic sections to construct depositional lithofacies and lithofacies associations for units in the PCC (after Miall, 1985; Blair and Mcpherson, 2008; Blair and McPherson, 2009). The following sections describe lithofacies associations and their interpreted lithofacies components. Example lithofacies and lithofacies associations are pictured in Figure 4, and the large-scale stacking patterns of lithofacies associations are presented in Figure 5.

S2.1 Alluvial Lithofacies Association

Alluvial fan lithofacies are ubiquitous within the PCC, and are similar to those described in previous publications (*e.g.* Blair and McPherson, 2009). In the PCC these lithofacies are composed primarily of cobble to boulder conglomerates interbedded with thin clean to muddy sand beds of varying lateral continuity (Figure 4m, n).

Lithofacies Gm: matrix supported gravel conglomerate

Lithofacies Gm is found throughout the PCC in continuous to laterally discontinuous beds of 10 cm to >1-3 m thickness. Gm matrix is brown to greyish green, sand- to silt-sized grains, with pebble- to cobble- to boulder-sized angular to subangular clasts. Lithofacies Gm usually lacks internal structure, but may contain faint stratification. Lithofacies Gm is interpreted to be the product of pseudoplastic, unconfined to channelized mud-supported debris flows.

Lithofacies Gc: clast supported gravel conglomerate

Lithofacies Gc is found throughout the PCC, and is often laterally continuous to discontinuous over 1s to 10s of meters, can be <10 cm to >3 m in thickness, is composed of angular and subangular pebble to boulders, with interstitial sand- and silt-sized grains. Clasts may be imbricated with evidence for bedload traction structures and faint stratification. Matrix in Gc is typically fine to coarse sand with little mud present. Lithofacies Gc is interpreted to be water-lain debris flow deposits, reworked debris-flow material, or sieve deposits. Gc is pictured in Figure 4m.

Lithofacies Sg: Granule-pebble rich sand

Lithofacies Sg occurs in the transition from fine-grained units to conglomerate alluvium in Section One in the south PCC. Granule- to pebble-rich coarse to medium sand in beds 10 cm – >1 m thick are faintly laminated or contain low-angle cross stratification. Traction structures indicate a water-lain origin, either subaerial or subaqueous deposition, while the association of these lithofacies to fine-grained lithofacies (discussed below) indicates a possible shallow lacustrine origin. Facies Sg is pictured in Figure 4a.

Lithofacies Sh: horizontally laminated or structureless sand

Lithofacies Sh is found throughout the PCC in laterally continuous to discontinuous beds ranging from 1 cm up to 3 m thickness. Laminations of very fine to medium-upper sand may be graded, or display load structures and deformation along bed contacts. Faintly bedded to structureless sand may exist in association with laminated beds. Lithofacies Sh is interpreted to represent unconfined sheetwash deposits in distal alluvial environment, possible waning stage subaerial dilute sediment flows. Lithofacies Sh is pictured in Figure 4a, d, and h.

S2.2 Lacustrine (and Mixed) Lithofacies Association

The Lacustrine Lithofacies Association is defined by finely laminated to featureless beds of fine silt to clay, and in section one, several meters of rhythmically bedded sandy turbidites. Lithofacies Sh, F, and Sg are the most common facies in the Lacustrine Lithofacies Association, and are pictured in Figure 4d – j.

Mixed lithofacies are present in both Alluvial and Lacustrine Lithofacies Associations, thus the term Mixed Lithofacies does not refer to a specific depositional environment, but rather an association of two mixed environments of deposition, stacked in vertical succession. Where fine-grained units interpreted as lacustrine (F, Sl) are interbedded with sands (Sl, Sg), and coarse-grained gravel conglomerates (Gc, Gm), we interpret a shallow or ephemeral lake with rapidly fluctuating environment of deposition. Examples of the Mixed Lithofacies are pictured in Figure 4a, 4b, and in the upper 1/3 of Figure 4k, and 4i.

Lithofacies F: Fine silt to clay

Lithofacies F crops out in laterally-continuous (100s m to km) deposits across the PCC, specifically in Section Two at ~115 – 119 m, and in Section One at ~19 – 28 m above the base of sections. Lithofacies F contains $CaCO_3$ and reacts to HCl, is white or greyish green or yellow in color, and composed of very fine sand, silt and clay-sized grains. sparse disarticulated ostracod or gastropod(?) fossils are observed in thin section. Bedforms include mm to cm scale horizontal, wavy, and crinkly lamination, minor ripple cross laminations, and reddish siderite filled root traces or burrows. Lithofacies F is commonly interbedded with Gm, and grades into Sf, Sl, and Gc, Gm up section. Lithofacies F is interpreted to represent a shallow to deep lacustrine environment. The complexity of preserved bedforms and dominant grain size argues against deposition in a fluvial or alluvial environment. Lithofacies F might best be termed a lacustrine marl.

Lithofacies Sc: horizontally laminated and contorted sand beds

Subaqueous sandy turbidity currents, stacked in sets of normally graded beds displaying contorted laminae, or dewatering structures. Sandy turbidites are subaqueous deposits interpreted to represent relatively deep lacustrine depositional environments. Lithofacies Sc is pictured in Figure 4h.

Lithofacies Gcr: rounded clast supported gravel conglomerate

Lithofacies Gcr is found at only one location, in the base of Section One (southern PCC; Figure 5). Gcr has the same sedimentary characteristics as Gc, with the notable difference of abundant subrounded to rounded pebble to cobble clasts and little matrix or when present loose coarse-grained sand and granule matrix. We interpret facies Gcr as wave reworked beach gravel deposits. Modern gravels near catchment outlets are typically angular with little rounding of clasts.

S3.0 SUPPLEMENTARY TEXT FOR MIXING MODEL

S3.1 Mixing model

We used a simple two-component (binary) mixing model to estimate proportions of various sediment sources necessary to drive observed CRN-derived paleodenudation variability. The CRN concentration (^{10}Be) in a binary mixture is dependent upon the starting concentration of end members ($C_{A, B}$) and the proportions of each end member present in a mixture (f_A):

$$(Eq. S1)\ C_m = C_A f_A + C_B(1 - f_A)$$

where C_m is the concentration of the binary mixture. We specified end-member concentrations (explained below), mixed end members, and used the resulting ^{10}Be concentration of mixed sediment, and the standard steady state catchment denudation equation (See Fig. 1 and text from Granger and Schaller, 2014) to calculate a denudation rate associated with each calculated value of C_m.

S3.2 Justification for end member CRN concentrations used in mixing model

The CRN-concentrations used in our mixture model were selected based on: (1) the average paleodenudation rate of the catchment, *i.e.* 36 mm/kyr, which corresponds to ~2.5x10^5 a/g SiO_2, a value assigned to the 'normal' sediment fraction, (2) the stored sediment CRN concentration was estimated by using the sum of the average concentration and a value that approximates surface production in the upper catchment (~1800 – 2000 m asl; ~16 atoms ^{10}Be/g SiO_2/yr) over ~15 kyr (*i.e.* close to the last glacial maximum), which yields ~5x10^5 atom/g SiO_2 for the 'stored' end member. We do not consider decay of ^{10}Be to be important this timescale. Finally, (3) for the mass wasting-derived CRN concentration, we assumed relatively shallow mass failures (~ 1 – 2 m) may entrain other material such as pre-existing regolith and bedrock. A value of 1x10^5 a/g SiO_2 was assigned. We acknowledge concentrations of mass wasting derived sediment may be extremely variable and dependent on the depth of detachment (Yanites et al., 2009). We also acknowledge that the resultant proportions of stored or mass wasting derived sediment necessary to drive denudation variability are dependent upon the prescribed CRN concentrations. Supplementary Figure 3 shows the resultant ^{10}Be-derived denudation rates associated with a range of end-member concentrations, and highlights the necessity for mixing of significant proportions (>35 – 45%) to drive the magnitude of variability observed in the PCC.

References

Blair, T.C., Mcpherson, J.G., 2008. Quaternary sedimentology of the Rose Creek fan delta, Walker Lake, Nevada, USA, and implications to fan-delta facies models. Sedimentology 55, 579–615. doi:10.1111/j.1365-3091.2007.00913.x

Blair, T.C., McPherson, J.G., 2009. Processes and forms of alluvial fans, Geomorphology of Desert Environments. doi:10.1007/978-1-4020-5719-9_14

Granger, D.E., Schaller, M., 2014. Cosmogenic Nuclides and Erosion at the Watershed Scale. Elements 10, 369–373. doi:10.2113/gselements.10.5.369

Miall, A., 1985. Architectural-Element Analysis : A New Method of Facies Analysis Applied to Fluvial Deposits. Earth Sci. Rev. 22, 261–308.

Supplementary Figure Captions

Supplementary Figure 1: Clasts of augen gneiss (World Beater complex) unique to the Pleasant Canyon catchment are found throughout measured sections of the Pleasant Canyon complex, in float and *in situ* within outcrops. **a**, **b**: Well-formed feldspar augen porphyroblasts in clasts of World Beater found in float in section 1. **c**, **d**: Examples of World Beater clasts found in outcrop in section 1.

Supplementary Figure 2.1: Correlations of lithostratigraphic measured sections and cosmogenic radionuclide (CRN) sample location within the Pleasant Canyon complex (PCC). **a**:

Photomosaic of outcrops of the PCC with CRN sample locations marked with red filled circles and associated text with sample numbers. White arrows denote samples taken from catchment outlets and modern CRN-derived denudation rates. **b**: Simplified lithostratigraphic sections one and two from the PCC with CRN results placed within stratigraphy.

Supplementary Figure 2.2: **a**: Syndepositional normal fault (~W-E striking) in north wall of Middle Park Canyon, approximately 200 m south of Section One. **b**: close up of three to five meters of throw on a steep normal fault (shown as dashed red line), down toward the basin in photo a. Subsidence via active normal faulting in part explains the expanded lacustrine strata in southern Pleasant Canyon complex.

Supplementary Figure 3: Proportion of mass-wasting derived or stored sediment vs. denudation rate. Horizontal grey dashed lines are the measured maximum and minimum of denudation rates for the Pleasant Canyon complex.

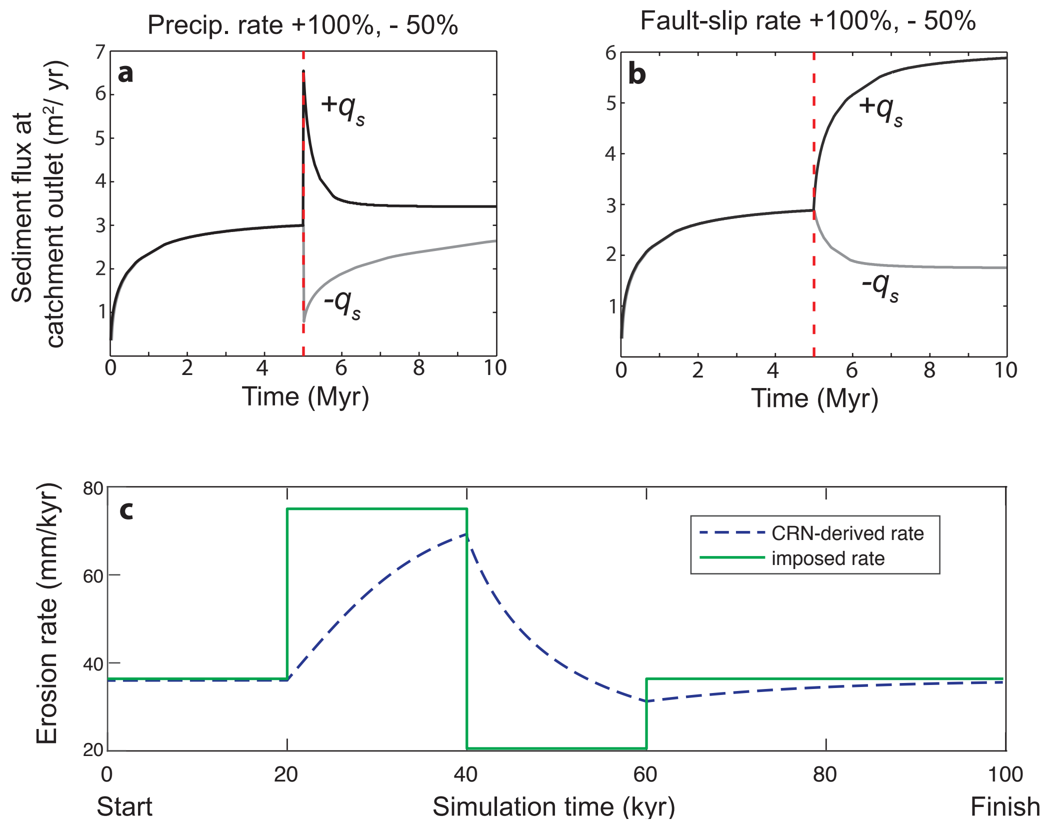

Precip. rate +100%, - 50%
Fault-slip rate +100%, - 50%
a
b
c
+q_s
-q_s
Sediment flux at catchment outlet (m²/ yr)
Time (Myr)
Erosion rate (mm/kyr)
CRN-derived rate
imposed rate
Start
Simulation time (kyr)
Finish

Figure 1

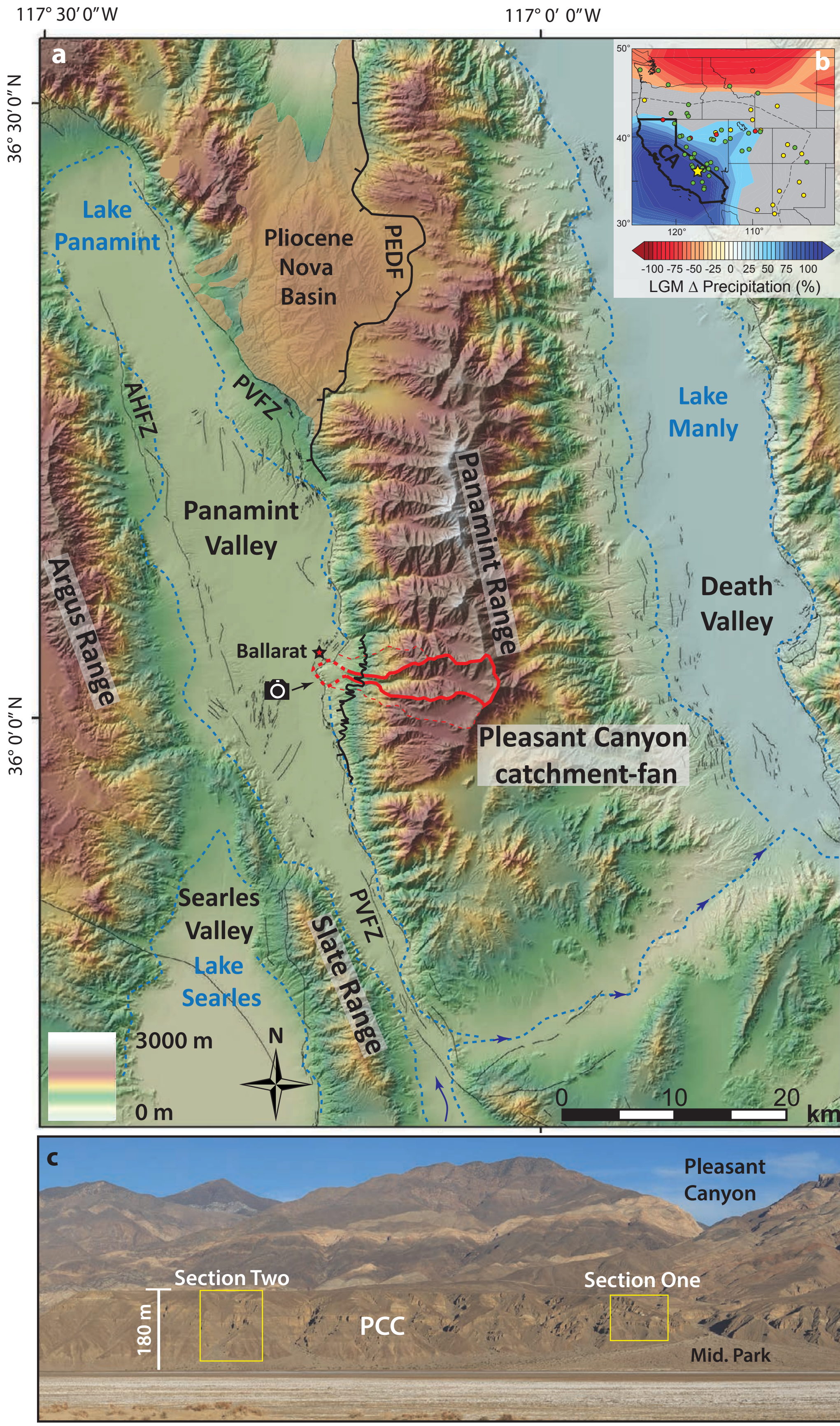
117° 30′ 0″W
117° 0′ 0″W
36° 30′ 0″N
36° 0′ 0″N
a
Lake Panamint
Pliocene Nova Basin
PEDF
PVFZ
AHFZ
Panamint Valley
Argus Range
Panamint Range
Lake Manly
Death Valley
Ballarat
Pleasant Canyon catchment-fan
Searles Valley
Lake Searles
Slate Range
PVFZ
3000 m
0 m
N
0 10 20 km
b
CA
-100 -75 -50 -25 0 25 50 75 100
LGM Δ Precipitation (%)
c
Pleasant Canyon
Section Two
Section One
180 m
PCC
Mid. Park

Figure 2

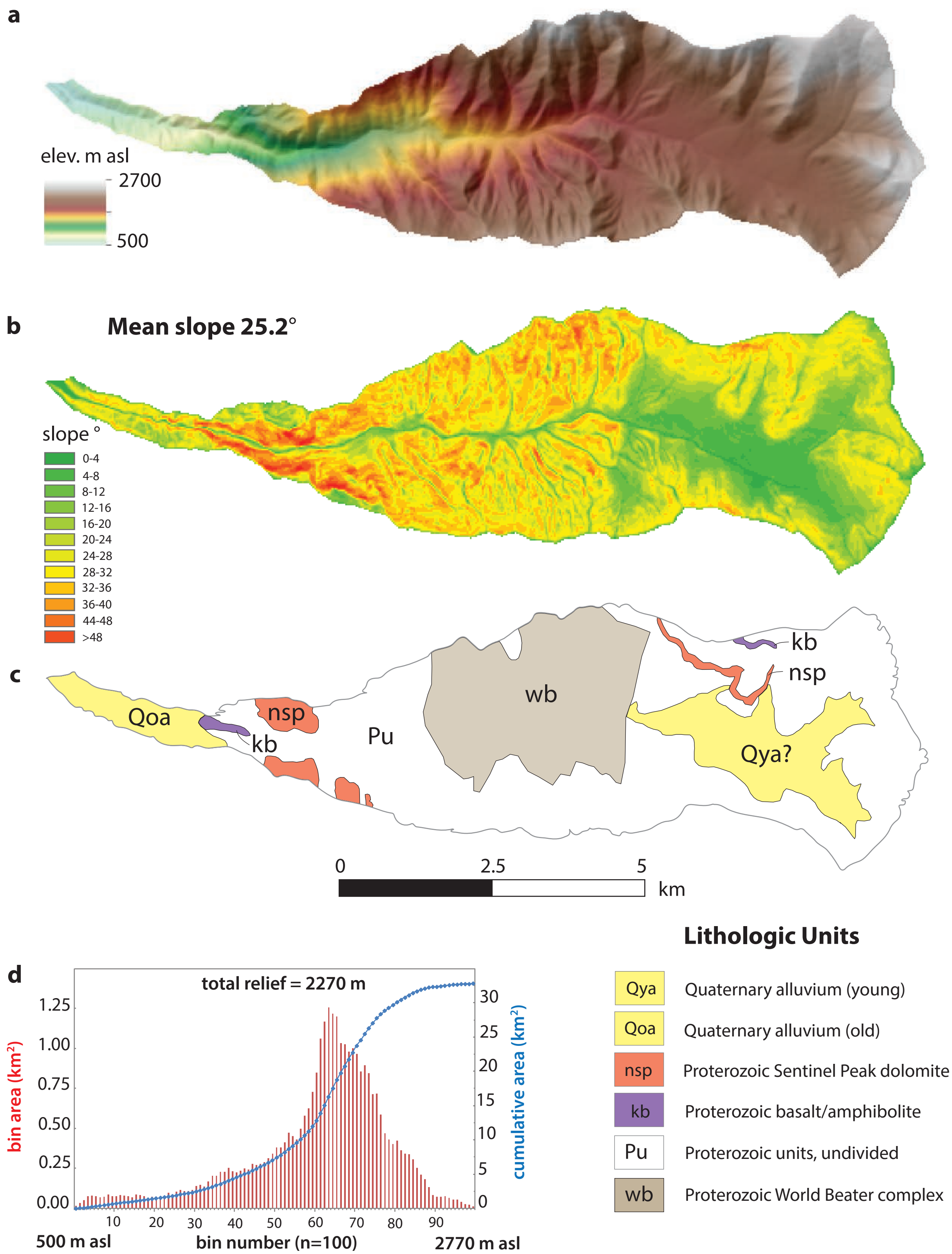
a
elev. m asl
2700
500
b
Mean slope 25.2°
slope °
0-4
4-8
8-12
12-16
16-20
20-24
24-28
28-32
32-36
36-40
44-48
>48
c
Qoa
kb
nsp
Pu
wb
kb
nsp
Qya?
0
2.5
5
km
Lithologic Units
Qya Quaternary alluvium (young)
Qoa Quaternary alluvium (old)
nsp Proterozoic Sentinel Peak dolomite
kb Proterozoic basalt/amphibolite
Pu Proterozoic units, undivided
wb Proterozoic World Beater complex
d
total relief = 2270 m
bin area (km²)
cumulative area (km²)
500 m asl
bin number (n=100)
2770 m asl

Figure 3

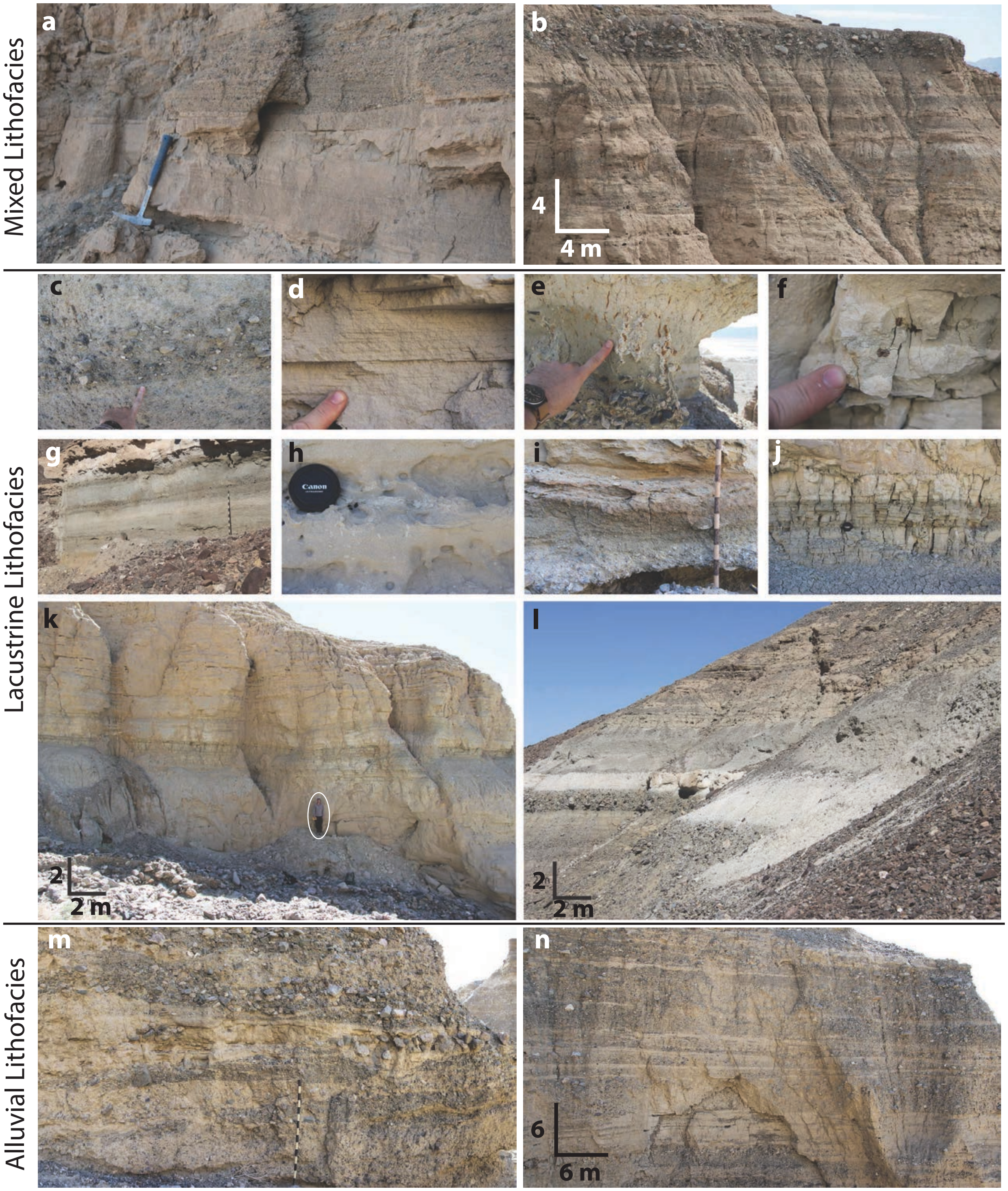
Mixed Lithofacies
a
b
4
4 m
Lacustrine Lithofacies
c
d
e
f
g
h
Canon
i
j
k
l
2
2 m
2
2 m
Alluvial Lithofacies
m
n
6
6 m

Figure 4

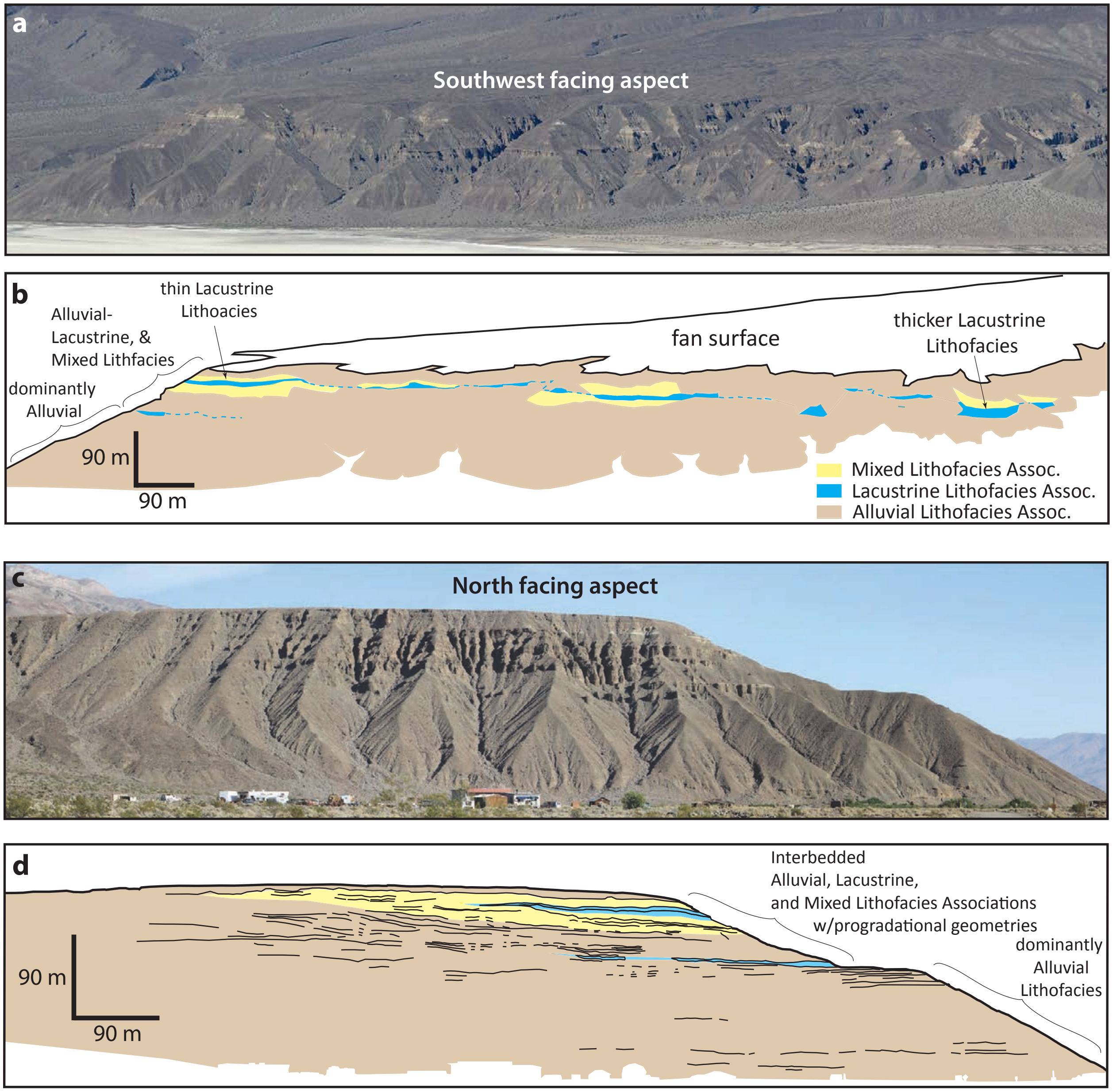
a
Southwest facing aspect
b
thin Lacustrine
Lithoacies
Alluvial-
Lacustrine, &
Mixed Lithfacies
dominantly
Alluvial
fan surface
thicker Lacustrine
Lithofacies
90 m
90 m
Mixed Lithofacies Assoc.
Lacustrine Lithofacies Assoc.
Alluvial Lithofacies Assoc.
c
North facing aspect
d
Interbedded
Alluvial, Lacustrine,
and Mixed Lithofacies Associations
w/progradational geometries
dominantly
Alluvial
Lithofacies
90 m
90 m

Figure 5

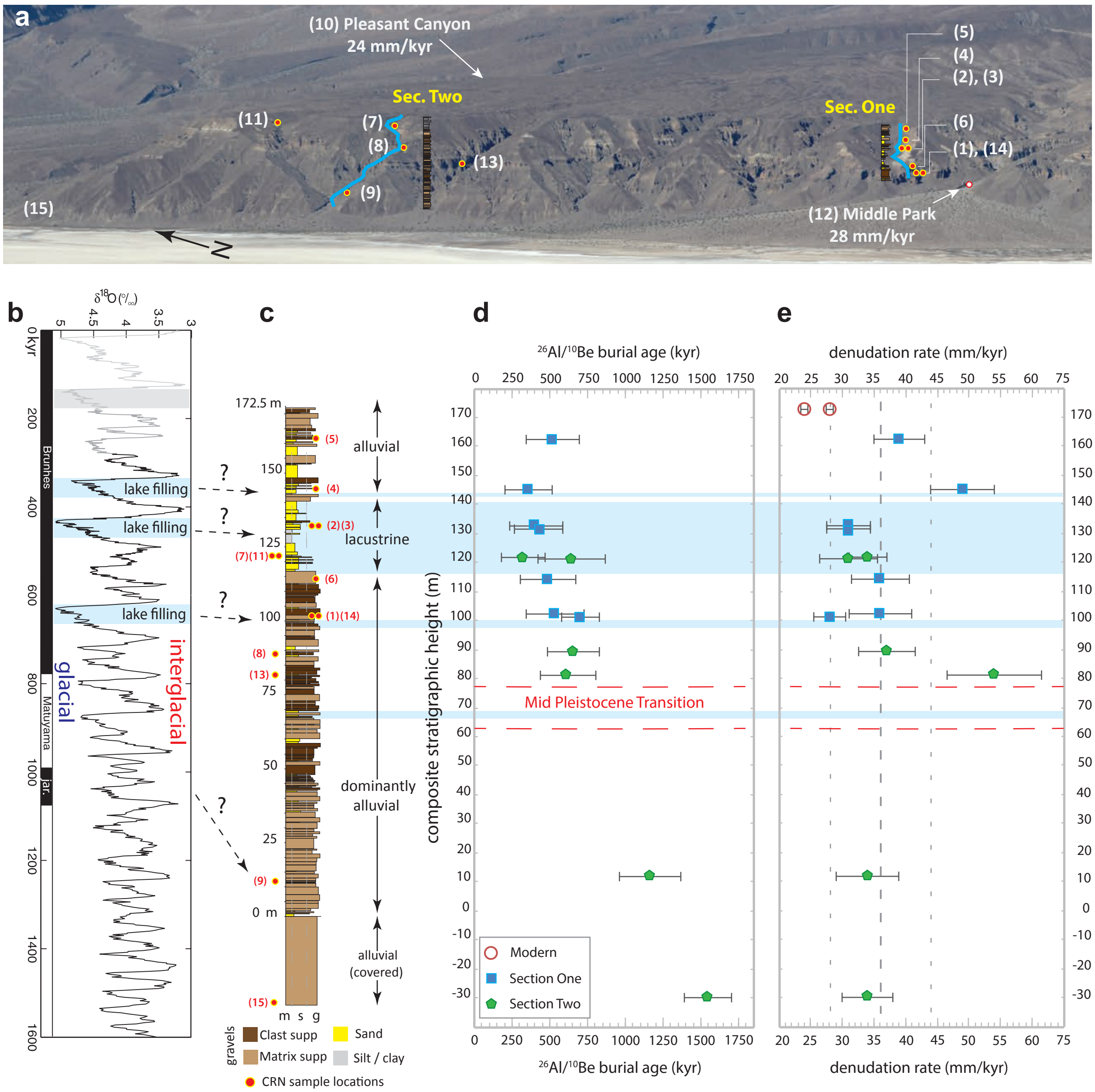
a
(10) Pleasant Canyon
24 mm/kyr
Sec. Two
Sec. One
(11)
(7)
(8)
(9)
(13)
(15)
(5)
(4)
(2), (3)
(6)
(1), (14)
(12) Middle Park
28 mm/kyr
N
b
c
d
e
lake filling
interglacial
glacial
Brunhes
Matuyama
Jar.
alluvial
lacustrine
dominantly alluvial
alluvial (covered)
Clast supp
Matrix supp
Sand
Silt / clay
CRN sample locations
Mid Pleistocene Transition
composite stratigraphic height (m)
^{26}Al/^{10}Be burial age (kyr)
denudation rate (mm/kyr)
Modern
Section One
Section Two

Figure 6

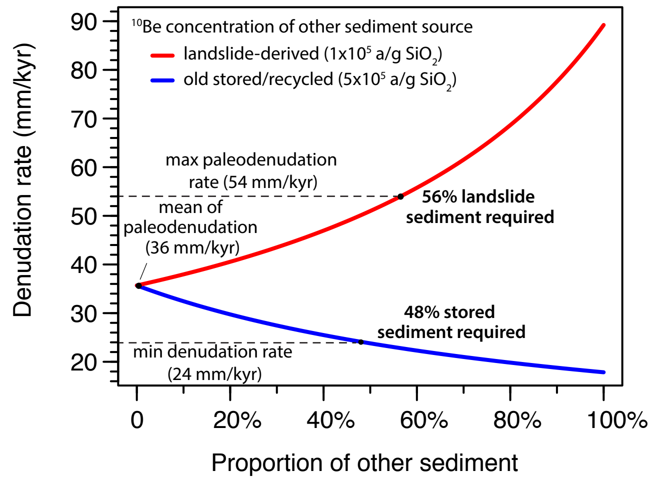

10Be concentration of other sediment source
landslide-derived (1x10^5 a/g SiO2)
old stored/recycled (5x10^5 a/g SiO2)
max paleodenudation rate (54 mm/kyr)
mean of paleodenudation (36 mm/kyr)
56% landslide sediment required
48% stored sediment required
min denudation rate (24 mm/kyr)
Denudation rate (mm/kyr)
90
80
70
60
50
40
30
20
0
20%
40%
60%
80%
100%
Proportion of other sediment

Figure 7

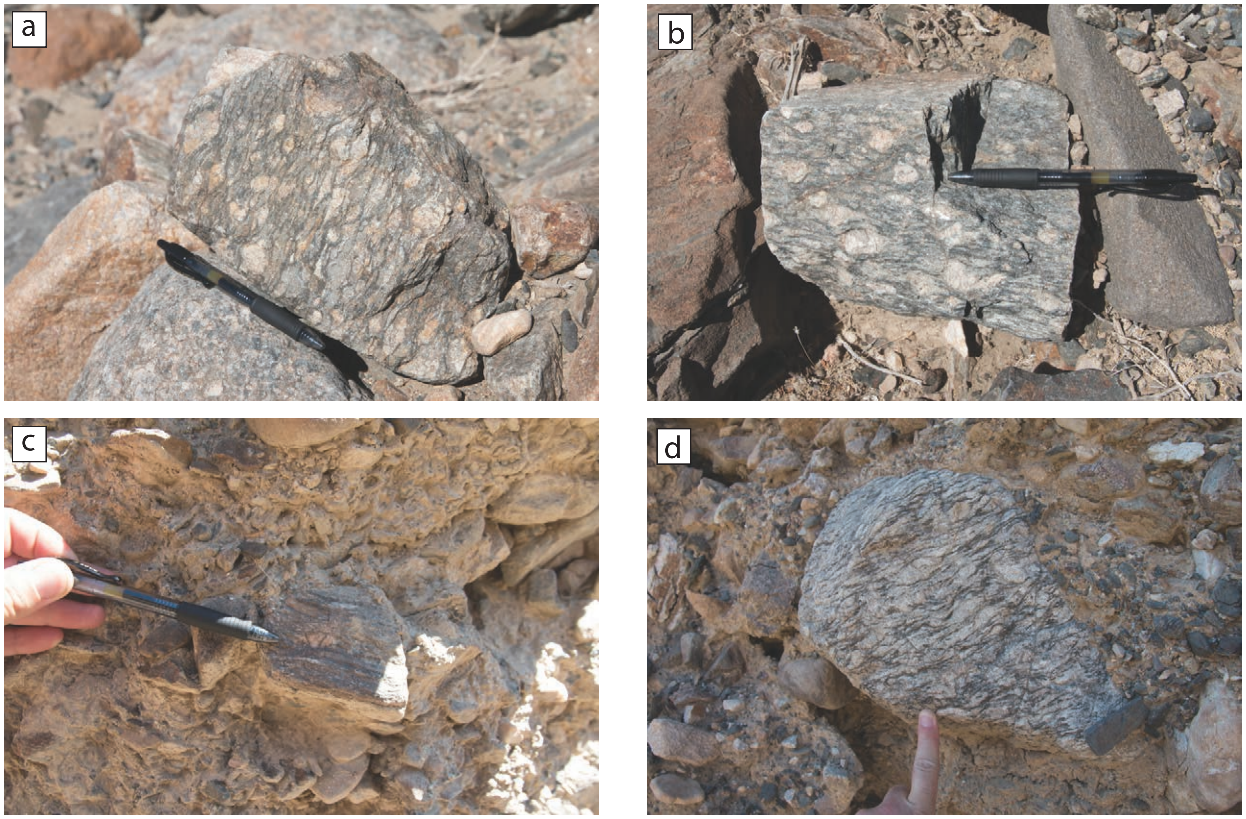

Suppl. Figure S1

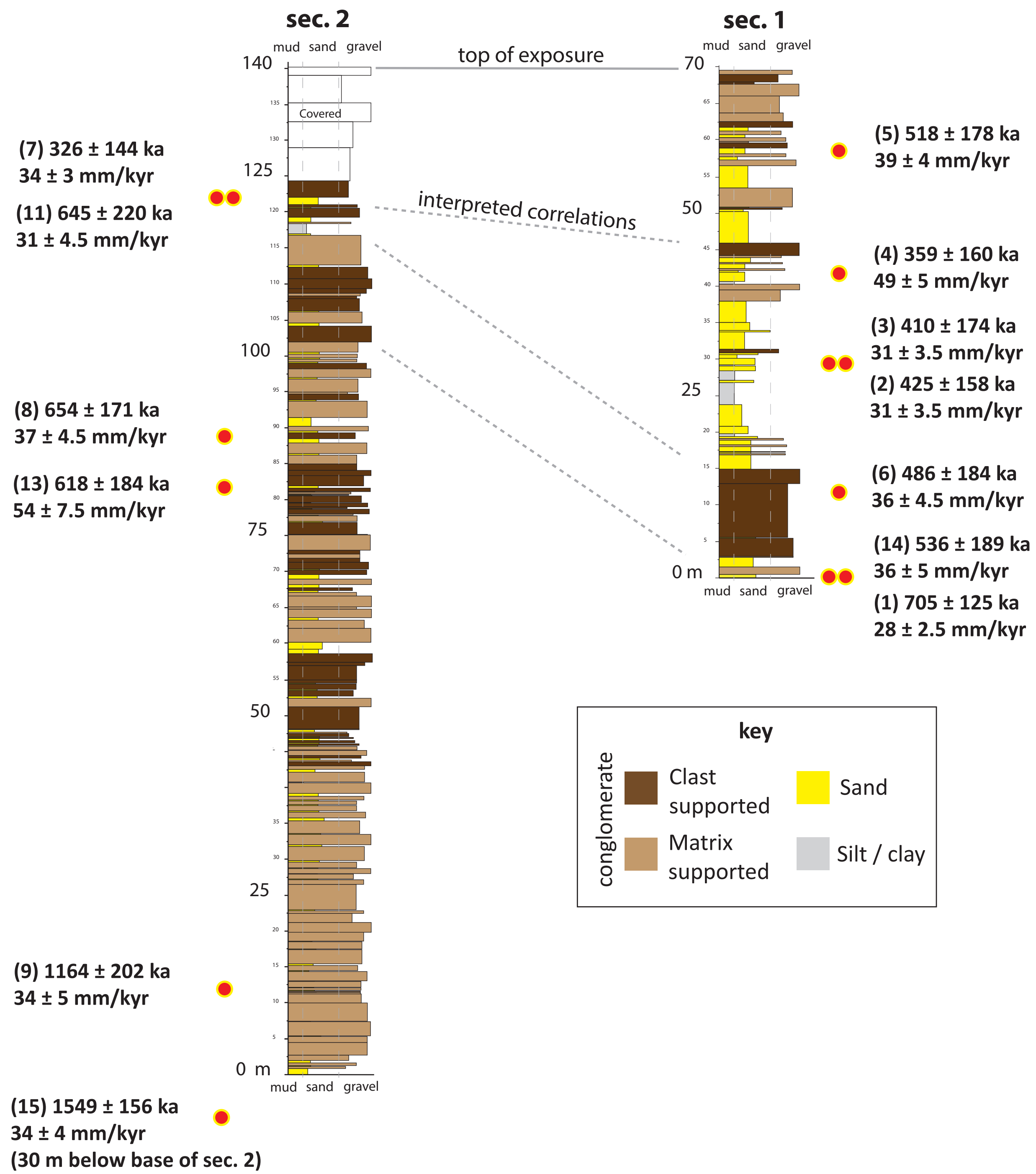

Suppl. Figure S2.1

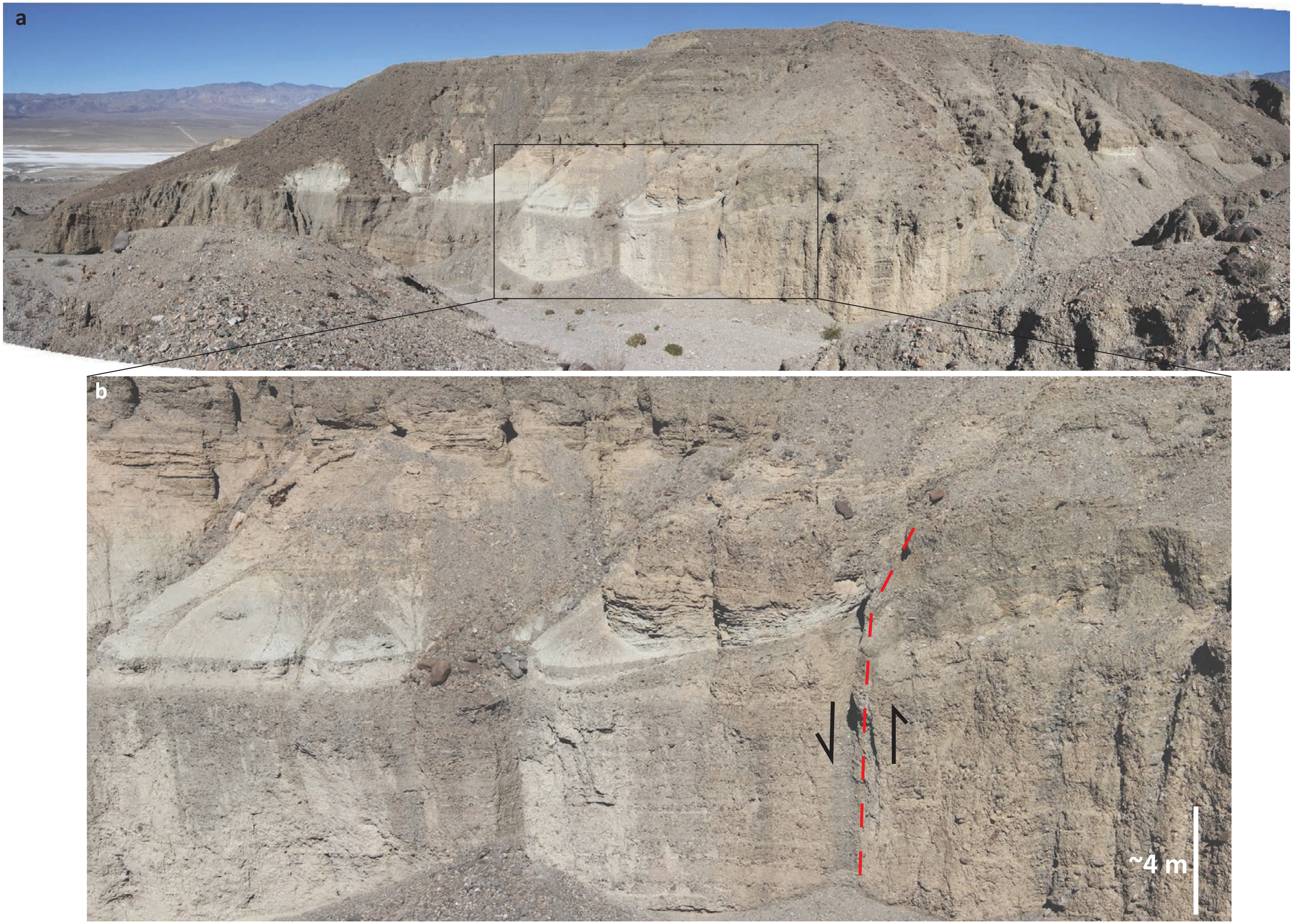

Suppl. Figure S2.2

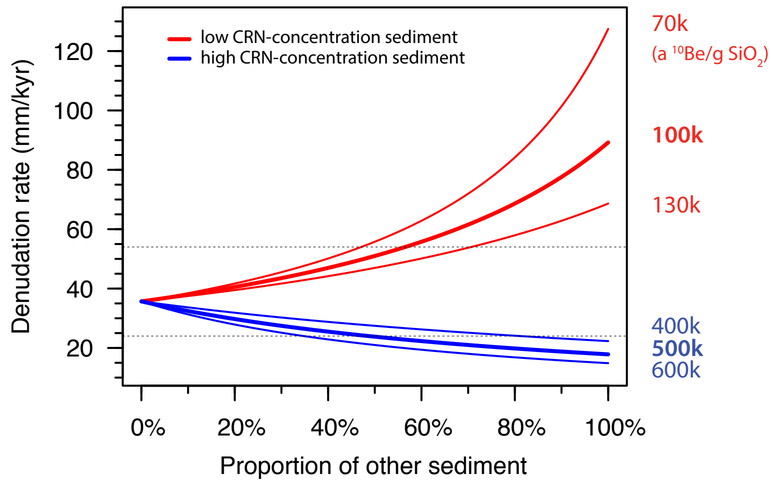

Supplementary Figure 3